Fall 2017

Mathematical Modeling for Predicting Chemotherapy and Nanoparticle Treatment Efficacy in Breast Cancer

Terisse Arielle Brocato

Terisse Brocato

Candidate

Biomedical Engineering

Department

This dissertation is approved, and it is acceptable in quality and form for publication:

Approved by the Dissertation Committee:

C. Jeffrey Brinker, Chairperson

Renata Pasqualini

Vittorio Cristini

Zhihui Wang

Ursa Glaberman-Brown

Wadih Arap

MATHEMATICAL MODELING FOR PREDICTING CHEMOTHERAPY AND NANOPARTICLE TREATMENT EFFICACY IN BREAST CANCER

By

TERISSE ARIELLE BROCATO

B.S. Biochemistry, University of New Mexico, 2011

M.S. Biomedical Engineering, University of New Mexico, 2016

DISSERTATION

Submitted in Partial Fulfillments of the
Requirements for the Degree of

Doctor of Philosophy Engineering

The University of New Mexico,
Albuquerque, New Mexico
May 2018

DEDICATION

This dissertation is dedicated to my family.

In particular

Grandma and Grandpa Uhl,

Mom, Dad, and Shayna,

Dustin, and all our future pups and kiddos.

All of you have been there through it all, my support, my rock, my motivation, and my guidance, and without you I wouldn't be where I am today or who I am.

ACKNOWLEDGEMENTS

I would like to thank my advisors, Dr. C. Jeffrey Brinker, for giving me the opportunity to work in his lab and do collaborative work with my other advisor, Dr. Vittorio Cristini. Throughout my graduate experience I was co-mentored by Dr. Renata Pasqualini, Dr. Zhihui Wang, Dr. Ursa Brown-Glaberman and Dr. Wadih Arap.

I would like to thank my advisors for serving on my dissertation committee, all mentioned above.

Thank you to my collaborators of whom I would not have been able to complete this research, Dr. Eric Coker, Dr. Reed Selwyn, Colin Wilson, Dr. Jennifer Saline, Dr. Lesley Lomo.

Thank you to my previous mathematical modeling group members in the Cristini/Wang group. Dr. Prashant Dogra who has worked next to me through it all, Dr. Joseph Butner, Dr. Romica Kerketta, Armin Day, and Dr. Yao-Li Chuang.

I would also like to thank all the members of the Brinker Lab that have helped me through my graduate experience. Dr. Jacob Agola, Dr. Paul Durfee, Dr. Darren Dunphy, Dr. Kimberly Butler, Dr. Rita Serda, Dr. Jason Townson, Dr. Yu-Shen Lin, Dr. Achraf Noureddine, Dr. Wei Zhu, Jimin Guo, Elizabeth Hjelvik, Edward Wyckoff, Mische Hubbard, Keoni Baty, Ayse Muniz, and Amanda Lokke.

I would also like to thank all the members of the Pasqualini/Arap Lab that have helped me, Dr. Andrey Dobroff, Dr. Marina Cardo Vila, Dr. Virginia Yao, Christy Tarleton, Amanda Leigh, Dr. Sara D'Angelo, Dr. Fortunato Ferrara, Dr. Fernanda Staquicini, Dr. Daniela Staquicini, Dr. Tracey Smith, Dr. Serena Marchiò, and Carolina Salmeron.

I would like to thank all my fellow classmates and friends Dr. Nesia Zurek, Kaylee Deutsch, Sommer Smith, Katie Gross.

Thank you to all my family, Robert Brocato, Terri Brocato, Shayna Brocato, Matthew Letter, Kaylie Letter, Carter Letter, and especially my amazing husband Dustin Mast, all of whom I wouldn't have made it this far without you all.

MATHEMATICAL MODELING FOR PREDICTING CHEMOTHERAPY AND NANOPARTICLE TREATMENT EFFICACY IN BREAST CANCER

By

Terisse Arielle Brocato

B.S. Biochemistry, University of New Mexico, 2011

M.S. Biomedical Engineering, University of New Mexico, 2016

Ph.D. Engineering, University of New Mexico, 2017

ABSTRACT

Breast cancer treatment response varies by subtype, treatment regiment, and additionally by vasculature characteristics. For this reason, breast cancer is a model disease for the development of both targeted therapy and prognostic and predictive biomarkers. Mathematical modeling allows for personalized patient specific prediction of treatment outcome based on parameters found to be important to the cancer type. Mathematical modeling is beneficial in providing insight into why cancer treatment fails and in what cases, additionally determining what characteristics result in a successful treatment. Presented in Chapter 1 is a scientific introduction and discussion focusing on representative modeling works specified towards breast cancer which give quantitative insight into chemotherapy resistance and how drug resistance can be overcome or minimized to optimize chemotherapy treatment. Demonstrated in Chapter 2, a modeling tool was created to predict the likelihood of response to neoadjuvant chemotherapy using patient specific tumor vasculature biomarkers measured in a total of 48 patients. To perform accurate and rapid throughput, a semi-automated analysis was implemented, improving on previous methods requiring hand-made

measurements. In effort to translate this model towards clinical practice, 48 patients undergoing neoadjuvant chemotherapy were evaluated, collecting clinically relevant data including pre- and post-treatment pathology specimens, and dynamic contrast-enhanced magnetic resonance imaging. Analysis of histology parameters, specifically radius of drug source divided by diffusion penetration distance (L/r_b), a normalization penetration distance, and blood volume fraction (BVF), provides a separation of patients obtaining a pathologic complete response (pCR) and those that do not, with 80% accuracy (p= 0.0269), providing a personalized approach to breast cancer treatment. Nanoparticles are shown to improve on cancer treatment efficacy, demonstrating improved cell kill when compared to free drug. Due to drug resistance and patient heterogeneity, patient outcome can vary greatly, in order to explore this phenomenon mouse treatment outcome relative to tumor and organ nanoparticle deposition is analyzed. A mouse study is presented in Chapter 3 as a proof-of-concept demonstrating the heterogeneous distribution of nanoparticles, and the improved cancer cell kill efficacy in an exponential fashion relative to accumulation of nanoparticles in the tumor. The combination of using nanoparticles as improved drug delivery vehicles, analysis of tumor biomarkers, and mathematical modeling to understand the underlying phenomena of treatment efficacy can be used in the clinical setting to help improve cancer treatment, and identify patients likely to respond well to differing and improved cancer treatment. Lastly, future directions are discussed in Chapter 4 whereby the application of chemotherapy, nanotherapeutics, and mathematical modeling may greatly improve and connect the theoretical and clinical side of cancer science.

TABLE OF CONTENTS

LIST OF FIGURES AND TABLES

LIST OF ABBREVIATIONS

AC- Doxorubicin (Adriamycin) and cyclophosphamide, chemotherapy agents

BVF- Blood volume fraction, ratio of blood vessel-to-tissue area in histopathology, or from MRI

CPS+EG- Pretreatment clinical stage and post-treatment pathologic stage (CPS score) as well as estrogen receptor status and tumor grade (EG) scores

DCE-MRI- Dynamic contrast enhanced magnetic resonance imaging

DFS- Disease-free survival

ER, PR, HER2- Tumor receptor status for estrogen, progesterone, and human epidermal growth factor 2

f_{kill}- Fraction of dead tumor, calculated as a function of L, r_b, and BVF

L- Diffusion penetration distance, the distance drug may diffuse away from a vessel and into the surrounding tissue at clinically useful concentrations

OS- Overall survival

pCR- Pathologic complete response

r_b- Radius of drug source, blood vessels in the tumor region

ROI- Region of interest

T- Paclitaxel (Taxol), a chemotherapy agent

TILs- Tumor infiltrating lymphocytes

TN- Triple negative hormone receptor status, tumor is negative for ER, PR, and HER2 receptors.

CHAPTER 1

INTRODUCTION

This chapter was adapted from:

Brocato, T.*; Dogra, P.*; Koay, E. J.; Day, A.; Chuang, Y.; Wang, Z.; Cristini, V. Understanding Drug Resistance in Breast Cancer with Mathematical Oncology. Current Breast Cancer Reports, 2014. 6(2): p. 110-120. (*Authors contributed equally to this work)

1.1 Overview

Breast cancer continues to be a major cause of death in women in the United States and globally.[1] The lethality of this disease is related to its robust ability to resist anticancer therapies.[2] Drug resistance, either acquired or intrinsic, is believed to cause 90% of all chemotherapy failures, and the 5- year survival rate for metastatic breast cancer in United State is only 26%.[3, 4] Multiple biological factors are believed to cause drug resistance, including genetic alteration, bypass mechanisms, altered effectors in DNA repair, pathway independent acquired resistance, pH alterations, and upregulation of efflux pumps in cellular membranes.[4-6] Another very important, but less-discussed reason that operates at a higher scale of organization is the existence of physical barriers that limit diffusive and convective drug transport in the required lethal drug concentrations to the regions of interest. The presence of dense extracellular matrix and interstitial hypertension in the tumor microenvironment and hostile conditions, marked by hypoxia and hyperacidity, affect drug penetration and drug efficacy, respectively[7-9], increasing tumor drug resistance when delivered in non-lethal concentrations to the tumor.

Mathematical modeling has been widely used as a method complementary to experimental investigations to provide insight into cancer initiation, progression, and invasion in the past several decades.[10, 11] Its importance is increasingly recognized for its capability to interpret and integrate the massive amount of data that experimental biologists are currently producing, especially in the era of data-intensive cancer research.[12] Modeling approaches can be briefly divided into 3 categories: discrete, continuum, and hybrid, ie, the combination of both (the reader can refer to[11, 13-17] for recent excellent reviews). Discrete models explicitly

represent individual cells (or part of a cell or a cluster of cells) in space and time, and then track and update their states and interactions according to predefined computational rules derived from experimental data. In contrast, continuum models represent the tumor as a continuous mass rather than as discrete components, and give information about the overall tumor morphologic behavior while neglecting the influences of individual cells. By drawing on the strengths of both continuum and discrete descriptions, hybrid modeling provides a more complete description of the tumor and its microenvironment, hence, having been accepted as the more desirable choice. Regardless of the modeling technique used, computational oncologists should note that the development of a successful cancer model is a long-term, integrative, and iterative process, where available experimental data are used to guide the model design and to validate the model.

Significant progress has been made in mathematical modeling of cancer drug resistance to understand how biological and physical factors of the tumor influence therapeutic outcomes. Mathematical models have applications that range from describing drug delivery, predicting cell kill from cytotoxic therapies, and anticipating tumor growth, among many others.[14] The ability to predict tumor-related outcomes aids the interpretation of experimental data and generation of specific biological/medical hypotheses. In this review, we will discuss the progress that has been made in mathematically describing fundamental processes in signaling networks and the tumor microenvironment, highlighting how the physical sciences can contribute to our understanding and treatment of breast cancer and other tumors.

1.2 Molecular Level Modeling

Overexpression of Efflux Pumps

Molecular level alterations and mutations can promote tumor formation and cellular drug resistance[13], which can cause hypersensitivity and overexpression of receptors, promoting tumor cell proliferation. For example, P-glycoprotein overexpression effectively lowers the intracellular concentration of chemotherapy, enabling cellular resistance to toxic drugs. Atari et al[18] studied drug resistance mechanisms of topotecan in breast cancer based on efflux pumps and drug resistance proteins. The primary efflux pump modeled, breast cancer resistance protein (BCRP), is known to be expressed in high concentrations in membranes of resistant tumor cells. A quasi-steady nonlinear drug kinetic model was developed in this study with consideration of a single cell's compartments, comprising the matrix, extracellular region, cell membrane, cytoplasm, and nucleus. This model demonstrates that topotecan resistance can be predicted from BCRP expression in the various compartments, which could aid the design of optimal dosing regimens.

P-glycoprotein Transfer between Cells

Cell-to-cell transfer of P-glycoprotein from resistant cells to sensitive cells not currently expressing P-glycoprotein is observed in cancer drug resistance.[19] Pasquier et al studied the role of P-glycoprotein expression in MCF-7 breast cancer cells using a time-dependent mathematical model based on a continuum population density function.[3] The model investigated and quantified how the overall drug resistance was affected by rates of cell proliferation and death,

P-glycoprotein induction and degradation, and P-glycoprotein transfer between cells. Their simulation results showed that the transfer of P-glycoprotein between breast cancer cells confers the multidrug resistance phenotype to cells not expressing P-glycoprotein.

HER2 Induced Drug Resistance

Breast cancer drug resistance of HER2 (human epidermal growth factor receptor; also known as ErbB2) targeting agents, including monoclonal antibodies for HER2-positive breast cancer, pertuzumab and trastuzumab, and/or a tyrosine kinase inhibitor, lapatinib, have been well studied.[20-22] Overexpression of HER2, found in 20%–30% of breast cancers[23], has a negative prognosis for survival.[24] Faratian et al used a systems biology approach to formulate a kinetic model that is predictive of resistance in response to receptor tyrosine kinase inhibitors. They found that the expression level of PTEN (a tumor suppressor protein) is the only significant predictor of survival by treatment with trastuzumab.[20] Kirouac et al used a multiscale network based pharmacokinetic and Pharmacodynamics model to determine the best combination treatment for HER2-amplified breast cancer cells, which resulted in the combination of trastuzumab, lapatinib, and an ErbB3 inhibitor, MM-111 being the most effective of the combinations tested.[21] Application of this model in a clinical setting will determine the best mixture of various chemotherapy drugs tominimize resistance in HER2-positive breast cancer. Niepel et al developed a mathematical model based on partial least-squares regression method to determine ligands that predict the response to treatment. Heregulin and ErbB3 were found to be good predictors of drug response. Clinically, this model can be used to determine biomarkers of drug sensitivity and resistance.[22] Vera et al also created a kinetic model, which determined chemoresistance based on genetic signatures of transcription factors E2F1 (positive

regulation of proapoptotic genes) and miR-205 (repression of antiapoptotic genes).[25] Results of this model demonstrate that genetic signatures can predict chemoresistance, helping to stratify patients for risk of therapy failure.

The Effect of the Cell Cycle on Chemotherapy

The cell cycle was found to play an important role in expression of P-glycoprotein and drug resistance. Roe-Dale et al[26] determined that breast cancer patients given sequential drug treatment of doxorubicin (DOX) followed by CMF (cyclophosphamide, methotrexate, and 5-fluoruracil) was more successful in reducing drug resistance than patients given alternating amounts of CMF and DOX in cycles. Chemotherapy drugs are found to be toxic in a cell-stage dependent manner, with DOX being more effective in the beginning and late portions of the cell cycle, and the CMF drugs being most effective in the beginning of the cell cycle. Specifically in,[26] modeling of the cell cycle and its effect on multidrug resistance through the use of successful sequential drug treatment compares 4 ordinary differential equation models (for drug treatment, cell cycle, drug resistance, and a combination of cell cycle and drug resistance, respectively), to determine importance of cell cycle and resistance on cell kill. The cell cycle and resistance model accounted for (1) cell cycle stage based on amount of DNA in a cell in a given stage and (2) cell cycle and accumulation of drug sensitivity due to P-glycoprotein. Their simulation results were consistent with patient and experimental data, with cellular drug resistance having a bigger impact than cell cycle stage.

1.3 Tissue-Scale Modeling

Overview: Biophysical Barriers to Drug Delivery and Therapeutic Resistance

Solid tumors (including breast cancer) are either drug resistant at initiation of chemotherapy, or become resistant with the progression of therapy, arguably because of selection pressure induced by cytotoxic agents on surviving cells.[27] As discussed in the previous section, the molecular principles of drug resistance play an important role in making cancerous cells refractory to treatment. Before these molecular/cellular mechanisms come into picture, 2 very critical aspects contribute to therapeutic resistance: drug delivery across the tumor and physiology of the tumor microenvironment.[9] The tumor microenvironment can be divided into 3 components: (1) cancer cells, (2) interstitium, which consists of stromal cells (fibroblasts and inflammatory cells) and the extracellular matrix (ECM), and (3) tumor microvasculature.[28] This environment is hostile to normal cells and is characterized by hypoxia, hypoglycemia, ATP depletion, acidosis, denser than normal ECM, and elevated interstitial fluid pressure (IFP) compared with normal tissue.[9, 29] This biochemical environment affects cellular behavior and drug chemistry, enabling tumor cells to survive chemotherapy. The microenvironment also poses a direct barrier to drug delivery. After a drug reaches the tumor microvasculature, extravasation from the microvasculature is the first challenge to overcome to enter the tumor interstitium.[30] Subsequently, drug molecules must penetrate through the abnormal tumor interstitium, cross the individual cancer cell membranes and eventually reach their subcellular targets. The transit from within the microvasculature to the inside of a cell is accompanied by biophysical and biochemical barriers of the microenvironment, and molecular barriers of cancer cells. Thus, the tumor microenvironment confers drug resistance in 2 ways, biochemical gradients and biophysical barriers [7–9, 27].[7-9, 27]

As a tumor grows in its vascular growth phase in a confined volume, it faces 2 kinds of solid stress: external stress and residual stress, applied by surrounding normal tissue and by the growing tumor, respectively. This stress is of the order of 1.3–13.0 kPa, sufficient enough for causing the collapse of blood and lymph microvessels. Vascular collapse of lymphatics leads to poor extracellular fluid drainage, whereas collapse of blood microvessels has implications for poor drug delivery and transport of oxygen, nutrients, etc.[31, 32] As indicated previously, tumor vasculature is drastically abnormal compared with healthy tissues. The "leaky" nature of tumor vasculature has been exploited in the passive targeting of drugs,[33] but a downside of this leakiness is the development of interstitial hypertension. Because of vascular hyperpermeability and poor lymphatic drainage, particularly at the center of the tumor, excess fluid accumulates in the interstitium, elevating the IFP. IFP equilibrates with microvascular pressure, which nullifies the pressure gradient required for extravasation of drug molecules on account of convection with the outgoing fluid. Thus, elevated IFP is a formidable barrier to convective transport, limiting the drug molecules from exiting the vascular compartment,[34, 35] and tends to exert an isotropic fluid-phase stress that also has direct implications for vascular collapse.[31, 36]

Following extravasation, the penetration through tumor interstitium occurs primarily via drug gradient-driven passive diffusion, and to some extent through convection. Usually, IFP tends to diminish pressure gradients on account of its fairly uniform elevation across the tumor, thus, diffusion remains the major determinant of interstitial migration of drug molecules.[35] However, diffusion of molecules through the interstitium to reach tumor cells at a distance from blood vessels is met by immense physicochemical resistance, which tends to hamper drug distribution.[7, 8, 37] Diffusion barriers within the interstitium occur on account of factors, such as

cellular adhesion, dense packing of tumor cells, composition of ECM, solid and fluid stress, and large distances between vessels.[38] The physicochemical properties of drugs, such as size and charge also affect their passage through the interstitium on account of their electrostatic, hydrodynamic, and steric interactions with the ECM.[39]

Clinical Trials Assessing Drug Delivery and Transport

Several trials have analyzed drug delivery in patients to variable degrees of sophistication to understand the factors that influenced how much drug reached the intended target. For example, gemcitabine delivery was measured for patients with squamous cell cancers of the head and neck,[40] but factors related to delivery were not assessed in this trial. The main goal of delivery measurement was to determine whether specific doses of gemcitabine were sufficient for detectable delivery. The transport-related changes after anti-angiogenic therapy have also been assessed, supporting the hypothesis of vascular normalization.[41] In a study conducted in breast cancer patients treated with doxorubicin, it was seen that drug did not reach all parts of the tumor tissue, and gradients were established with more drug in the periphery of the tumor than its center. This effect was more pronounced in tumors with dense packing of cancer cells.[42] The effects of paclitaxel and doxorubicin on interstitial fluid pressure and oxygenation were measured in a trial of neoadjuvant chemotherapy for patients with breast cancer, showing that paclitaxel improved the transport properties of the tumors whereas doxorubicin did not. This provides rationale to optimize the sequence of chemotherapies.[41] In another study done on mouse models of various solid tumors, similar trends of exponential decrease in doxorubicin concentration with increasing distance from nearby blood vessels were observed.[43] These studies demonstrate nonuniformity

of drug distribution across the tumor and indicate potential involvement of biophysical barriers in thwarting chemotherapy.

We recently published a first-in-kind clinical trial of intraoperative gemcitabine infusion for patients with resectable pancreatic cancer.[44] The objectives were to measure the incorporation of gemcitabine into the DNA of tumor cells and understand the factors that influence delivery. We used semiquantitative scoring of the pathology to assess stromal score and the staining levels of the cellular transporter of gemcitabine, hENT1,[45] which may be associated with outcome in pancreatic cancer. We also developed a mathematical model to describe the changes in density during routine contrast-enhanced computed tomography (CT) imaging of patients with pancreatic cancer. We discovered that gemcitabine delivery to the cellular DNA could be described by multi-scale transport phenomena, as characterized by both the stromal score and hENT1 levels. Furthermore, the CT-derived transport properties also correlated with the drug delivery. We extended our CT transport analysis to 110 patients who received protocol-based neoadjuvant gemcitabine-radiation for resectable pancreatic cancer, and found that the pre-therapy CT-derived transport properties correlated with pathologic response and survival. Thus, transport properties of pancreatic cancer describe the delivery of, response to, and survival after gemcitabine-based therapies.

Extending these methods to patients with breast cancer would help to identify the major biophysical barriers to drug delivery. Such efforts could aid the design of new therapeutic strategies that overcome these physical impediments. If combined with mathematical oncology approaches, these clinical trials could provide a mechanistic understanding of drug delivery for each patient.

Vascular Supply of Drugs

A mathematical model by Sinek et al[46] accounted for the morphologic and vascular heterogeneity of tumors, and predicted the effectiveness of anticancer agents. The model employed a multiscale tumor growth and angiogenesis simulator[47] based on an adaptive finite element mesh by Cristini et al[48] for simulating tumor growth and response to chemotherapy administration. Simulation results showed that tumor microenvironmental factors relevant to drug, oxygen, and nutrient distribution led to variations in tumor response to chemotherapy, implicating this variable drug delivery as a cause of therapeutic resistance. This model can potentially serve as a tool for predicting in vivo pharmacokinetics of anticancer agents.

Baish et al[49] developed a mathematical model using fluorescent vascular images to determine the effect of architectural, physiological and branching irregularities of tumor vasculature on the delivery of therapeutic agents and nutrients. By calculating δ_{max} (maximum distance from the nearest blood vessel) and λ (a measure of shape of voids between vessels) from vascular images, the authors showed that the model predicted the amount of "material" (eg, nutrients and therapeutic drugs) and the time required for the material to reach its destination. The model predicted diffusion in irregularly shaped domains and evaluated the efficacy of therapeutic agents that induce "vascular normalization".[50] This mathematical model accounted for the existence of diffusion barriers pertinent to irregular vasculature and can be used to quantify the effect of such impediments on drug delivery. Thurber et al[51] also developed a model using in vivo images of drug distribution around tumor vasculature from murine tumor models. Their model predicted drug distribution profiles along the vasculature with intermittent blood flow. This model may be used as an assessing tool for predicting

conditions where tumors may not receive therapeutic amounts of administered drug in clinical practice, and, thus, might be inclined to resistance.

Transvascular Extravasation of Drugs

Stapleton et al[52] modeled convective drug transport across tumor microvasculature and tumor interstitium to study the transport of liposomal drug delivery that implements the enhanced permeation and retention (EPR) effect by accounting for transvascular and interstitial fluid dynamics.[53] The model provided a theoretical framework for predicting intratumor and intersubject variations in liposomal accumulation because of variations in EPR based on microenvironmental physiological factors. Wu et al[54] extended a previously developed vascular tumor growth model[55] by incorporating IFP and interstitial fluid flow (IFF), lymphatic drainage, and vascular leakage. The model revealed the effects of elevated IFP on drug, nutrient and oxygen extravasation, and tumor growth, as it indicated that interstitial pressure caused microvascular collapse and influenced tumor growth through nutrient and oxygen deprivation.

The extravasation of molecules tends to be affected by steric, hydrodynamic and electrostatic interactions between molecules and pores of leaky vessels. Stylianopoulos et al[56] studied interactions between nanoparticles and negatively-charged pores to predict the existence of an optimum value of surface charge density. The model was applied to various sizes of nanoparticles and found that for every nanoparticle size, there is a value of surface charge density above which electrostatic forces become dominant and leads to a steep increase in transvascular flux. Such a mathematical model would play a critical role in guiding the design of nanotherapeutic formulations for anticancer drug delivery.

Drug Diffusion through Tumor Interstitium

Stylianopoulos et al[57, 58] modeled the tumor interstitium to predict the effects of repulsive electrostatic interactions and fiber network orientation on the diffusion of charged drug molecules through the matrix. Their model predictions suggested that electrostatic interactions between fibers and drug molecules/nanoparticles tended to slow down diffusion. This prediction explained the observation that neutral particles diffuse faster in comparison to charged particles. Simulating fiber network orientation with varying degrees of fiber alignment, their analysis demonstrated that the overall diffusion coefficient was not affected by network orientation; however, diffusion anisotropy was predicted as a result of structural anisotropy. Diffusion anisotropy becomes even more significant with increasing degree of fiber alignment, particle size, and fiber volume fraction.

As an extension to a 3-dimensional multispecies nonlinear tumor growth model by Wise et al.,[59] Frieboes et al[60] developed a model based on in vitro spheroids and monolayers of breast cancer cells that incorporates the biophysical barriers for drug and nutrient diffusion and provides a quantitative relationship between tumor phenotype and its response to chemotherapy. The model simulates impeded diffusion of drug, oxygen, and nutrients, and correlates it to poor response to chemotherapy on account of both poor drug delivery and lack of nutrients required for cellular proliferation. The model can be instrumental for clinical use in predicting the effect of chemotherapy on a tumor of known phenotype. Das et al[61] also modeled the 3-dimensional aspects of the tumor microenvironment in the context of the diffusion of interferon-γ through the tumor interstitium. The mathematical model predicted the limited success of immunotherapy in breast cancer on account of the diffusion barriers.

Recently, Pascal et al[62] developed a mathematical model based on the physical laws of diffusion to predict the fractional tumor killed because of chemotherapy. The important parameters in the model were volume fraction occupied by tumor blood vessels and their average diameter, as measured from histopathology. Drug delivery to cells and subsequent tumor cell kill were assumed to be mediated by these microenvironmental properties. The model predicted tumor cell kill in colorectal liver metastases and glioblastoma, using patient-specific histopathology data (Figure 1.1). Thus, it can be used to develop individualized treatment strategies that account for the amount, frequency, and delivery platform of drugs and other cytotoxic therapies.

Biochemical Gradients within Tumor Microenvironment

For cancer cells to remain alive and actively dividing, it is critical that their metabolic requirements be met. When the metabolic load supersedes the supply of oxygen and nutrients, hypoxic tumor cells tend to induce angiogenesis to maintain a constant supply of oxygen and nutrient rich blood. Despite neovascularization, there is a continual gap between demand and supply; aggressive tumors might have high microvascular density but still have significant hypoxia and acidosis because of inadequate perfusion.[63] Because of aberrations in the vessel wall integrity, tumor blood tends to become hyperviscous. As a result of solid and fluid stress within the tumor, vascular collapse can occlude the flow of blood, leading to high resistance to blood flow and, thus, insufficient perfusion.

The distribution of tumor vasculature within the tumor is heterogeneous, creating anisotropy in perfusion in terms of both space and time. As a result of heterogeneity of blood perfusion, drug

does not reach uniformly to all parts of the tumor leading to a population of cancer cells being untouched, or only moderately touched by the cytotoxic agent. Tumor tissue tends to develop gradients of oxygen level, pH, glucose, ATP and rates of cancer cell proliferation across the tumor. A direct implication of hypoxia is G1/S-phase cell cycle arrest.[64] Because of low extracellular pH, weakly basic drugs tend to get protonated and exhibit lower cellular uptake.[65, 66] Eventually these biochemical gradients result in reduced sensitivity to cell cycle specific cytotoxic agents.[67] In extension to a mathematical model[68] that predicted the extent and location of quiescent cells in multicellular spheroids, Venkatasubramanian et al[69] incorporated cell cycle progression, nutrient and drug transport limitations, and pharmacodynamics and pharmacokinetics to predict the effect of tumor microenvironmental heterogeneity and hostility on drug cytotoxicity. Their simulation results suggest a therapeutic strategy: optimizing molecular weights of drug molecules to reach an optimum diffusion coefficient that is neither too small to be cleared from blood before effective penetration, nor too large to limit effective drug retention.

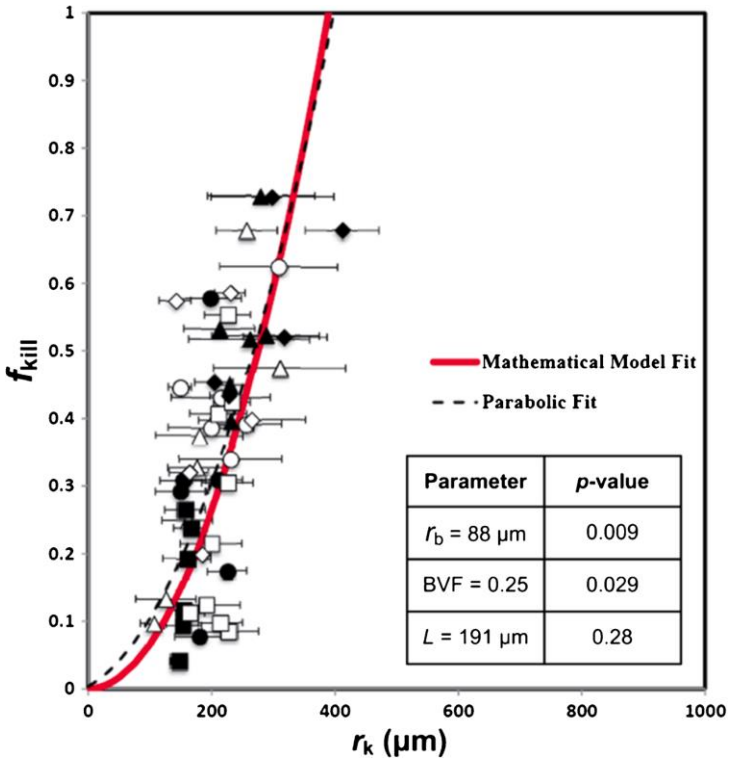

Figure 1.1 Patient fraction of tumor killed regression relative to thickness of dead tissue. Results of fitting the model[62] to patient data by a regression analysis. Fraction of tumor killed f_{kill} and thickness of dead tumor regions r_k were measured in 49 histopathologic sections of colorectal cancer metastatic to liver after chemotherapy. Quadratic least-square fit (dashed curve; R^2= 0.92) and least-square fit (red curve; R^2=0.94) of the model are shown. Biologically realistic parameter values obtained from the fit are shown in the inset table. This analysis demonstrates that the model agrees with the distribution of the patient data. Adapted with permission from.[62] *BVF* blood volume fraction, r_b blood vessel radius, *L* diffusion penetration distance

<u>Overcoming Physical Barriers with Nanotherapeutics</u>

Current standard therapies for breast cancer are efficacious to a limited extent.[61] Nanotherapies may confer advantages over conventional drugs in overcoming therapeutic resistance. Possible advantages include delivering higher concentrations of drug, promoting greater drug uptake by tumor cells, overwhelming drug efflux pumps, accumulating drug in tumor vasculature, and causing less toxic effects on the patient.[70, 71] Silica nanovectors with doxorubicin were able to overcome therapeutic resistance and outperform traditional therapies against hepatocellular carcinoma in vitro because of their ability to carry much higher concentrations of drug. This promoted a higher amount of overall drug uptake and greater overall cell kill.[72] Nanoparticles (NPs) also use far less drug overall, allowing for the potential to deliver larger quantities of NPs or even higher drug concentrations with still fewer negative cytotoxic effects.[73] A study done with osteosarcoma found that NPs loaded with doxorubicin were more effective because they had higher levels of accumulation in solid tumors and they were able to deliver drug to the nucleus of the tumor cells.[74] This accumulation may be attributed to longer circulation times because of their small size and specific surface ligands. These small NPs can specifically target tumor endothelium with low or high affinity, enabling them to distribute throughout the tumor, or accumulate at the inlet, depending on which is desired in a specific treatment.[70, 71] Many researchers also contribute NPs effectiveness to its ability to circumvent therapeutic resistance efflux pumps such as P-glycoprotein, preventing drug loss from tumor cells.[72, 74]

CHAPTER 2

MATHEMATICAL MODELING TO PREDICT RESPONSE TO NEOADJUVANT CHEMOTHERAPY USING BREAST CANCER VASCULATURE CHARACTERSTICS

This chapter was adapted from:

Brocato, T.*; Glaberman-Brown, U.*; Wang, Z.*; Selwyn, R.; Wilson, C. M.; Wyckoff, E. F.; Lomo, L.; Saline, J.; Pasqualini, R.; Arap, W.; Brinker, C. J.; Cristini, V. Mathematical Modeling to Predict Response to Neoadjuvant Chemotherapy Using Breast Cancer Vasculature Characteristics. Submitted to *Science Advances*. (*Authors contributed equally to this work)

2.1 Overview

In the United States, breast cancer is the most common female cancer and is the second most common cause of cancer death in women [75]. While major advances have been achieved in treatment of early stage breast cancer, many women still die from the disease. The use of neoadjuvant chemotherapy has emerged as a promising approach to evaluate the efficacy of chemotherapy in patients with early stage breast cancer. Improved patient survival is correlated with complete eradication of invasive tumor in the primary breast lesion and lymph nodes (pathologic complete response, pCR) by neoadjuvant chemotherapy. This has been demonstrated in many studies, including National Surgical Adjuvant Breast and Bowel Project (NSABP) protocol B18, in which 1,523 women with early stage breast cancer were randomly assigned to preoperative versus postoperative anthracycline based chemotherapy [76]. There was no difference in disease-free survival (DFS) or overall survival (OS) at 5 years among either treatment group. However, in the 683 women that received neoadjuvant treatment, outcomes were significantly better in women who achieved a pCR compared to those without a pCR (5 year OS 87.2% vs. 76.9% - 78.4% p=0.06, DFS 83.6% vs. 60.3% -71.7% p = 0.0004) [77]. Data also support that women who have a significant response to neoadjuvant chemotherapy but do not achieve a pCR have improved long-term outcomes. Mittendorf et al. described and validated a novel breast cancer staging system for assessing prognosis after neoadjuvant chemotherapy on the basis of pretreatment clinical stage (CS), estrogen receptor status and grade (EG), and post-treatment pathologic stage (PS), known as the CPS+EG score [78]. The ability of the CPS + EG score to stratify outcomes was confirmed in both internal and external cohorts, with a score of $\leq$ 2

corresponding with a 5 year disease-specific survival (DSS) ranging from 88% to 96%. In those with a score $\geq$ 3 the DSS dropped significantly, ranging from 72-88% [78].

In order to maximize the utility of the neoadjuvant therapy strategy, there is a clinical need for tools to predict patients that are likely to respond to neoadjuvant cytotoxic chemotherapy, thereby allowing a personalized approach to cancer treatment. Here, we present a novel integrated study based on a mathematical model utilizing tumor vasculature characteristics paired with patient data analysis to predict response to neoadjuvant chemotherapy.

Response to chemotherapy is known to vary by breast cancer subtype and chemotherapy regimen. Unfortunately, neoadjuvant cytotoxic chemotherapy with conventional anthracycline and/or taxane based regimens (the standard of care for most patients with early breast cancer) results in a pCR in only a minority of patients [79]. For example, in SWOG 0012, 185 patients with locally advanced breast cancer were treated with standard AC (doxorubicin and cyclophosphamide) given every 21 days for 5 cycles, followed by weekly T (paclitaxel) for 12 weeks [80]. Overall pCR rate was 21%. However, in patients with hormone receptor (HR)-negative tumors, the pCR rate was 29% compared to 11% in patients with HR-positive tumors. Tumor specific biomarkers predicting response have been explored, including tumor infiltrating lymphocytes (TILs). TILs correlate with improved outcomes in several cancer types, including colorectal, ovarian, esophageal, renal, lung, pancreatic, and breast cancer [81-83]. The presence of TILs in diagnostic needle core biopsy in women with early stage breast cancer was shown to be an independent predictor of response to neoadjuvant chemotherapy [84], as was TIL density [85].

We hypothesize that tumor vasculature characteristics may similarly be a biologic predictor of response to chemotherapy. This hypothesis was previously examined in a series of integrated modeling studies evaluating the prediction of cancer treatment outcome based on drug diffusion and physical properties of the tumor [72, 86-92]. We hypothesized that diffusion barriers prevent drugs from reaching the tumor, a mechanism that (among others) underlies drug resistance [93]. Our mechanistic mathematical model for predicting tumor response to chemotherapy (denoted by f_{kill}, i.e., the fraction of tumor killed due to therapy) has been validated retrospectively in patients with colorectal cancer (CRC) metastatic to the liver [86]. The model has demonstrated the ability to predict tumor response to chemotherapy treatment using three drug perfusion and diffusion related histology parameters: blood volume fraction (BVF) in the tumor, the distribution of blood vessels (r_b), and the drug diffusion distance in tumor tissue (L). These three parameters are tumor and patient specific, and therefore need to be measured on an individual basis. Additionally, pre-chemotherapy contrast-enhanced computer tomography (CT) perfusion scans were used to calculate the model parameters, followed by correlation of model predictions to post treatment results. We observed an average relative error of ~15% when comparing f_{kill} predicted from histopathology vs. f_{kill} predicted from pre-treatment CT-derived patient specific BVF values. Here, we sought to expand on this model by applying it to breast cancer, evaluating histology and dynamic contrast-enhanced magnetic resonance imaging (DCE-MRI) data. It is worth noting that, in the previous retrospective study [86], two major parameters (r_b and L) were solved for in the f_{kill} model; whereas, in the present study, all model parameters were directly measured using a

semi-automated computer program further described below. See **Figure 2.1** for an overview of our research protocol.

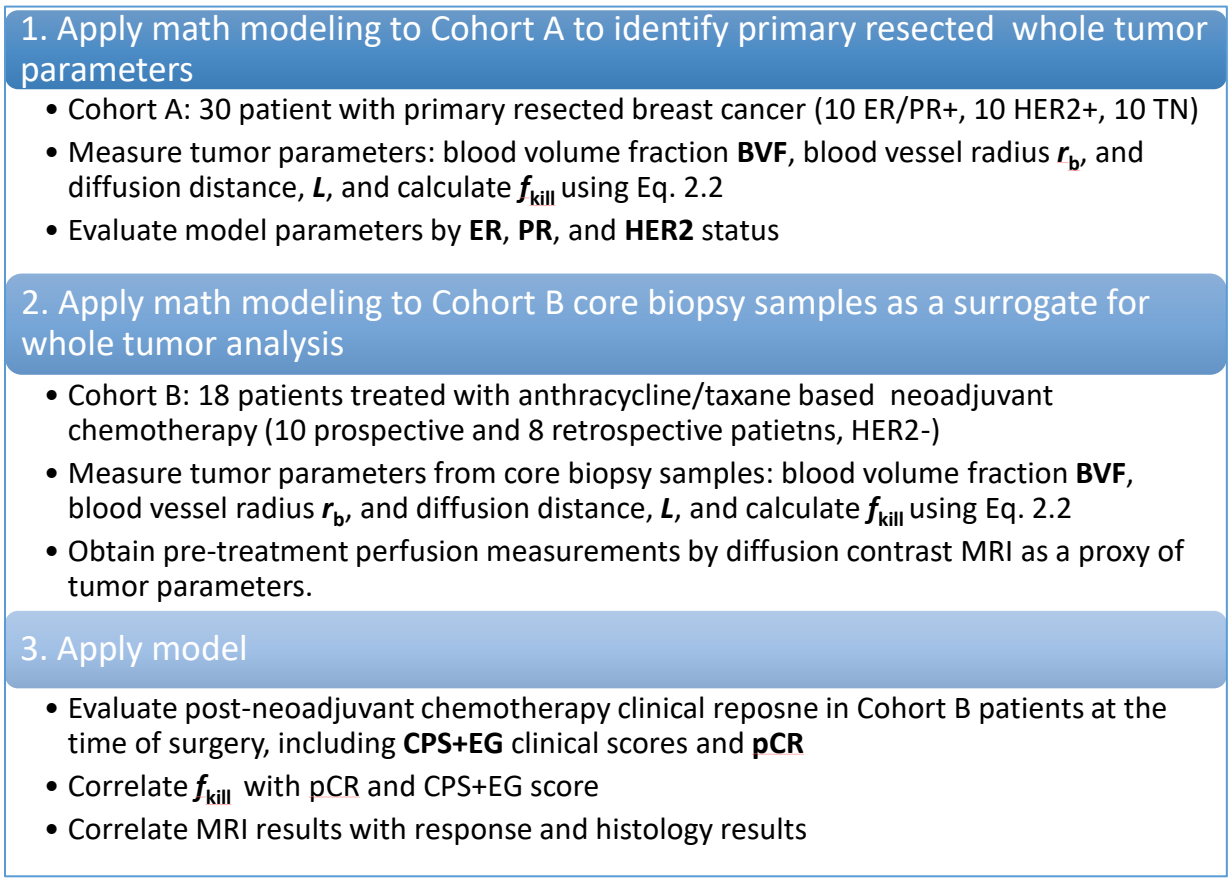

Figure 2.1. Research protocol.

2.2 Results

Needle Core Biopsy Feasibility

We first sought to determine the feasibility of using diagnostic needle core biopsies to mathematically predict f_{kill} in women with stage II-III HER2$^-$ breast cancer infiltrating ductal carcinoma receiving neoadjuvant anthracycline/taxane based chemotherapy. Toward this goal, histological analysis to obtain model parameters was performed retrospectively on whole

tumors from 30 patients who underwent upfront lumpectomy (primary surgery without prior systemic therapy), Cohort A in **Figure 2.1**. Model parameters obtained from the whole tumor in these patients were subsequently compared to a similar analysis of histologic samples from 18 patients' pre-neoadjuvant chemotherapy diagnostic needle core biopsy, Cohort B in **Figure 2.1**; the results are shown in **Figure 2.2**. Nonlinear regression was performed using the f_{kill} model and patient histological parameters specific to each patient's tumor vasculature. Cohort A has a higher BVF than Cohort B likely due to the whole tumor section analysis in Cohort A, while Cohort B had of the more limited core biopsy samples. Due to shape alone, the tissue section from a whole tumor block results in a larger highly vascularized tissue region (perimeter of tumor) for Cohort A when compared to the cylindrical shape of a core biopsy for Cohort B. The patient samples for both cohorts fall along the same regression line; correlation for Cohort B analysis between $f_{kill}(BVF_{biopsy}, (L/r_b)_{biopsy})$ vs. $f_{kill}(BVF_{biopsy}, (L/r_b)_{fitting})$ results in $r = 0.7042$. This demonstrates that core biopsy samples can be used to determine histological parameters representative of the whole tissue region. Subsequent analysis demonstrated that L/r_b measurements provide significant distinction between patients in Cohort B achieving a pCR and those without a pCR, **Figure 2.3**.

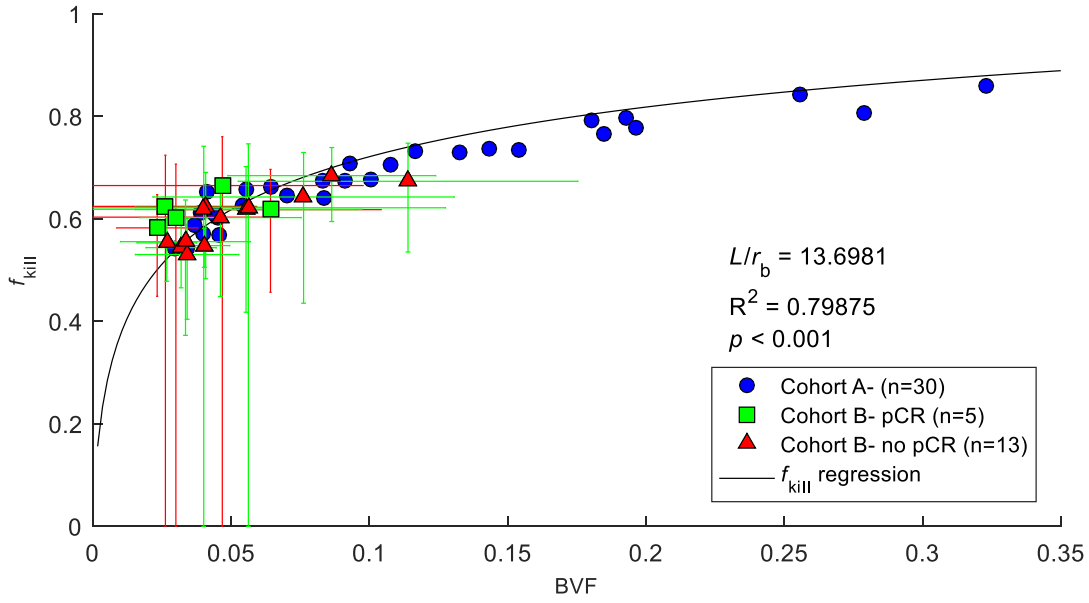

Figure 2.2. Model analysis. Cohort A: 30 retrospective patients undergoing primary surgery without prior systemic therapy analyzed using histology semi-automated analysis and mathematical model. Cohort B: 18 patients receiving neoadjuvant chemotherapy are shown to distinguish patients with pathologic complete response (pCR) vs. those without a pCR. Each point is a patient's predicted f_{kill} using averages of BVF, r_b, and L measured directly from surgically resected tumor tissue stained with CD34 by immunohistochemistry. The black line shows an f_{kill} regression line calculated from Eq. 2.2 with optimized parameter L/r_b = 13.6981, R^2 = 0.79875. The f_{kill} regression line includes fitting of all treated and not treated patients (n = 48). Error bars are calculated based on error in BVF measurements and their respective variation that it causes when plugging into the f_{kill} equation (Eq. 2.2).

Receptor Status Non-Separation between Patient Groups

There was no differentiation between patient groups (hormone receptor positive tumors, HER2 positive, and triple negative breast cancer) in the Cohort A based on an ANOVA test. These patients are thus grouped together for f_{kill} mathematical modeling, as shown in **Figure 2.2**.

Clinical Scoring System and Separation between Clinical Outcomes by L/r_b

CPS+EG scores range from 0–6, where patients having a CPS+EG $\leq$ 2 have a 88% chance of being alive 10 years following diagnosis [78]. We were unable to discriminate between responders and non-responders using a CPS+EG score of $\leq$ 2. However, analysis of histology measurements, specifically L/r_b, provides a separation of patients achieving a pCR from those that do not, with 80% accuracy shown in **Figure 2.3**. A positive correlation is seen between pCR and L/r_b, validated in **Figure 2.5**. A *t*-test on L/r_b between pCR and no-pCR patients indicates p= 0.0269 (significance level $\alpha = 0.05$, two-sided parametric test, assuming equal variances). A single patient was identified as a clear outlier, potentially as a result of a dense population of TILs, (a known independent predictor of response to neoadjuvant chemotherapy, although not all patients in Cohort B with TILs had a similarly positive responses to therapy. By model parameters, this patient was predicted to not have a pCR. We note that this benchmark L/r_b value is likely to be cancer-type specific, the determination of which would require the evaluation of a lager patient cohort.

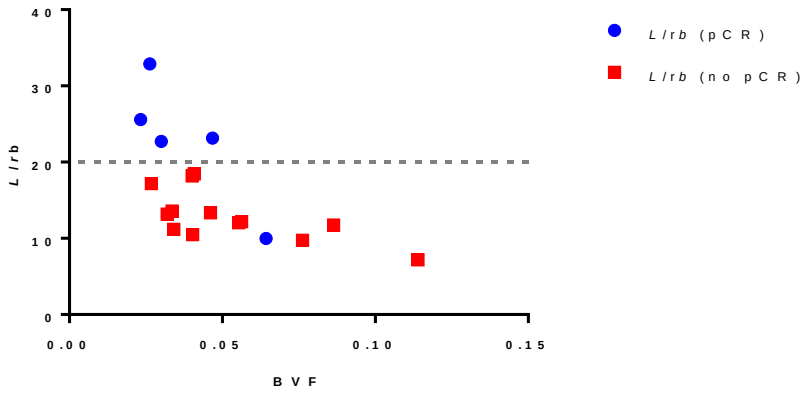

Figure 2.3. Histological parameters and their correlation. pCR and L/r_b demonstrate a positive correlation. Dashed grey line based on L/r_b (approximately 20) separates patient groups with 80% accuracy.

DCE-MRI Area under the Curve (AUC) Association to Histology L/r_b

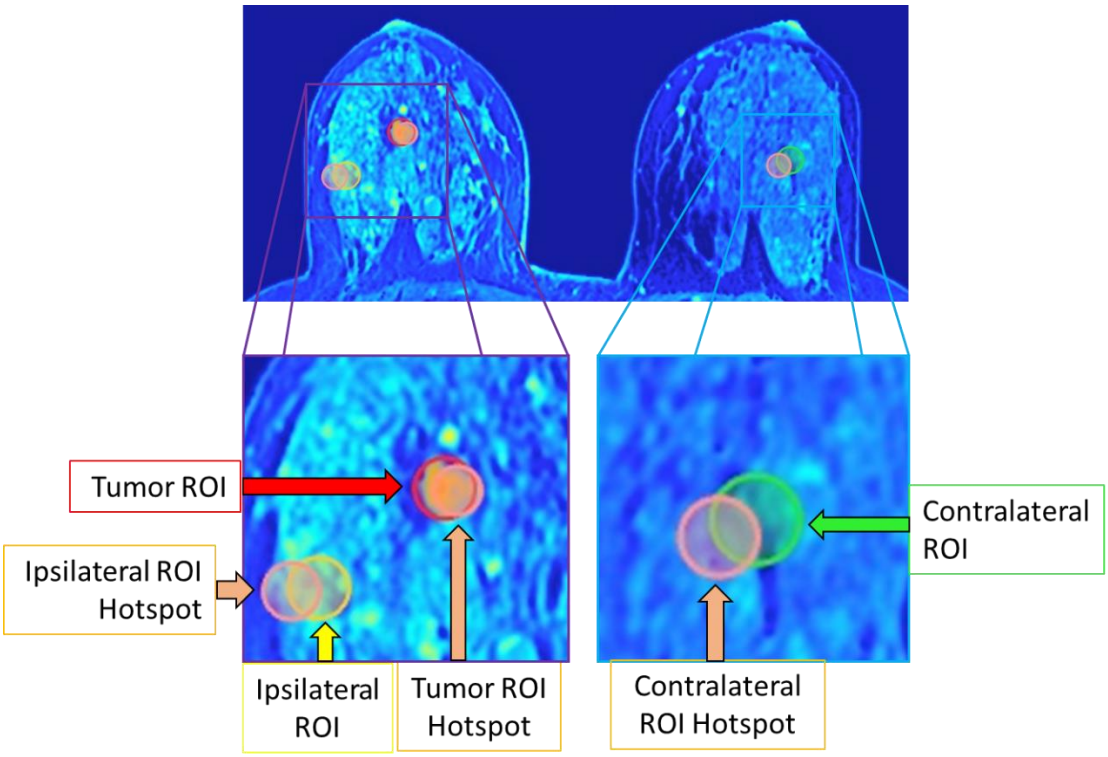

Figure 2.4. DCE-MRI regions of interest (ROIs) for incorporation into Figure 2.5. Image shown is an Area Under the Curve (AUC) Map for all MRI time points for which data are taken, 0-5.5 minutes, with all Regions of Interest (ROIs) being spherical. All hotspot ROIs are defined as the max $1cm^3$ spherical ROI with the center point included in the main ROI drawn. Ipsilateral ROI is shown as an alternative control ROI if both breasts on the patient contain a tumor, in this case the Ipsilateral ROI Hotspot will be used in place of the $AUC_{\text{Contralateral ROI hotspot}}$.

$$AUC_{hotspot}(\text{tumor/control}) = \frac{AUC_{\text{Tumor ROI hotspot}}}{AUC_{\text{Contralateral ROI hotspot}}} \quad \textbf{[Eq. 2.1]}$$

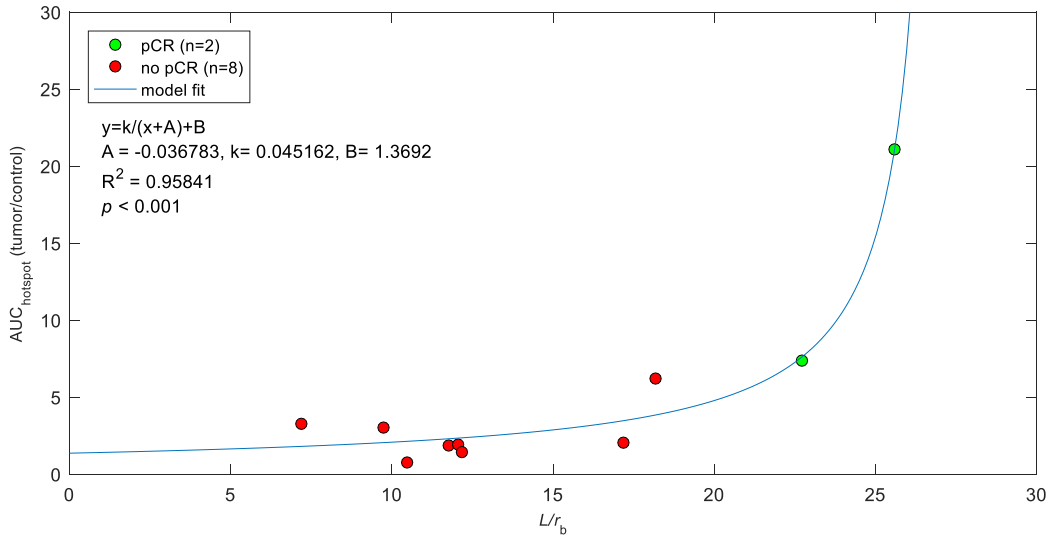

Figure 2.5. Response to neoadjuvant chemotherapy and DCE-MRI in Cohort B. CD34 stained core biopsy samples measured for L/r_b (radius of blood vessel: r_b, tissue diffusion penetration distance: L) and its relation to DCE-MRI area under the curve (AUC) analysis, time points 0 - 5.5 minutes, taken for the hotspot region of the tumor normalized to the contralateral breast's hotspot in the same tissue region on the contralateral breast (considered to be normal breast

tissue). Coefficients *A*, *B*, and *k* are fit to determine best values for prediction between L/r_b and its relation to DCE-MRI area under the curve (AUC) analysis using a reciprocal function. *A*, *B*, and *k* are coefficients specific to stage HER2 negative, stage II-III breast cancer treated with neoadjuvant treatment.

Histology and DCE-MRI measurements demonstrate a link shown in **Figure 2.5**, and an example for where the data comes from in **Figures 2.4 (Eq. 2.1)** and **Figures 2.7**. As described, diagnostic core biopsy samples were analyzed to obtain L/r_b. pCR and L/r_b demonstrate a positive correlation which is demonstrated in **Figure 2.3** additionally. An area under the curve map (AUC) in the tumor region was used to estimate tumor blood perfusion from DCE-MRI data, as previously demonstrated in Pickles et al [94]. In order to obtain quantitative data from DCE-MRI, a region of interest (ROI) must be used; here, the hotspot of the tissue ROI (tumor or control tissue) was used to determine the max perfusion in that tissue region. Tissue hotspot analysis has been shown to be a good predictive tool for DCE-MRI [94], and was demonstrated to be predictive of treatment outcome short-term (AUC map of hotspot 3x3 pixel region) when looking at pre-treatment and early in treatment [94, 95]. By correlating AUC obtained from MRI measurements to L/r_b obtained from histology, we can better predict which patients will have a response to neoadjuvant chemotherapy prior to getting treatment. Furthermore, this can be performed without using core biopsy samples, useful given the often limited specimens obtained at the time of biopsy.

2.3 Discussion

The work presented here demonstrates that it is feasible to evaluate predictive biomarkers, specific to primary breast cancer vasculature in a patient specific manner, using semi-automated analysis. The quantities: r_b, BVF, and L are shown to be reliably predictive of tumor f_{kill} when obtained from either mastectomy/lumpectomy specimens or diagnostic needle core biopsy in stage II-III breast cancer patients.

One of the limitations in our previous research in CRC [86] was that the histology parameters, L and r_b were solved for in the f_{kill} model (Eq. 2.2). Here, we have updated this method by measuring these values (L, r_b, and BVF) directly from histology. BVF was previously measured from hematoxylin and eosin stained slides [86]. In the current study, we utilized vasculature specific staining to allow for better visualization, increasing the accuracy of analysis. Measurements were previously done by hand which is prone to human error. In the present study, a semi-automated computer program was created to allow for increased accuracy in measurements while reducing time required for analysis. The automated analysis allows for rapid throughput; in this study over 4000 patient images were analyzed. Furthermore, in this study we correlated clinically relevant treatment response assessments (pCR and CPS+EG) with model parameters measured. Some limitations of this study include differences in vasculature staining, which was minimized using a computer automated staining protocol, additionally tissue staining was performed in the minimum number of staining batches possible. Core biopsy samples are taken through one entrance point, which may limit the tumor region being tested. Attempts are made to take into account such tumor heterogeneity by taking 3-4 biopsies which extend out from the entrance point. Additionally, patient clinical DCE-MRIs should contain a normalization method during acquisition to allow for a controlled method for

all patient MRIs with T1 mapping and magnetic field correction additionally with scans taken frequently (every 3 seconds and more spaced out between scans for 90 seconds through 5.5 minutes post contrast). In order to obtain a BVF from MRI, at the time of scanning, arterial input function might be evaluated to obtain additional data from the MRI and make core biopsy histology not necessary for model prediction.

Tumor vasculature is a chaotic labyrinth of malformed and destabilized vessels that are structurally and functionally impaired [96]. Jain et al. has argued that drug delivery to tumors can be enhanced through tumor vessel normalization and reduced interstitial fluid pressure induced by anti-angiogenic therapy [50]. A low L/r_b value for pCR patients is indicative of a more "normalized" baseline tumor vasculature, explaining improved response to chemotherapy in this subset of patients. Normal tissue has regularly spaced (or separated) blood vessels which increases the value L, and therefore lowers the L/r_b parameter. Patient tumors with a high L/r_b values tended to have "pooled blood", or regions with highly vascularized tissue, severely limiting blood and drug delivery to poorly vascularized tumor regions.

DCE-MRI analysis resulted in AUC providing the most information regarding patient response from the data set provided. Hotspot ROI AUC analysis provided the best correlation to treatment outcome, when compared to looking at the whole tumor using 3D spherical ROI and a tumor ROI. Thus, the greatest perfusion region seems to be the best predictor of treatment outcome. Although hotspot analysis dictates outcome, the average tumor analysis typically leads to the same conclusion as well. Application of this model for clinical use at an initial diagnostic stage will allow for non-invasive prediction of tumor outcome, whereby likelihood pCR can be estimated early in the course of treatment, using flowchart **Figure 2.6**.

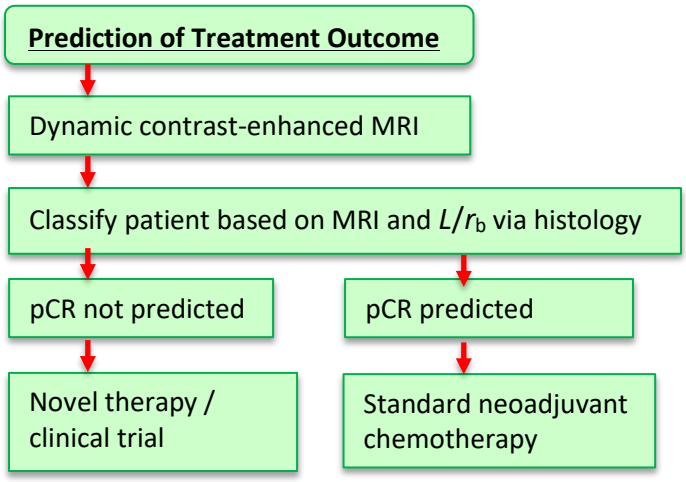

Figure 2.6. Prediction of treatment outcome flowchart using both MRI and tumor histology from diagnostic biopsies.

Our next steps will expand upon these results through inclusion of more MRI measurements with additional time points, including MRIs that will be taken after the patient's second neoadjuvant chemotherapy treatment. This is expected to provide a tool to determine early on if the patient is likely to responding to standard treatment, allowing personalized therapy. We also plan to investigate if and how we can use MRI as a surrogate for histology in the mathematical model parameters to predict treatment outcome.

2.4 Methods and Materials

Patient Cohorts.

Patient cohort A: 30 patients who underwent upfront surgical resection for invasive adenocarcinoma of the breast (without prior systemic therapy). 10 hormone receptor positive tumors (ER/PR+), 10 HER2 positive (HER2 amplified) tumors (HER2+), and 10 triple negative tumors were selected for retrospective histological analysis. See Histology and Histology Semi-automated Analysis sections below.

Patient cohort B: 18 women with HER2 negative stage II-III infiltrating ductal carcinoma of the breast receiving neoadjuvant chemotherapy with modern anthracycline / taxane based chemotherapy. 10 patients were treated and evaluated for model parameters prospectively, with an additional 8 patients evaluated retrospectively. Final analysis of the 18 patients was performed in aggregate. 6 of 18 patients had hormone receptor positive tumors, while 12 patients had triple negative tumors. Pre-treatment diagnostic core biopsy was used for Histology Semi-automated Analysis (see below for details). Pre- and post-treatment magnetic resonance imaging was performed per standard of care. All patients received a standard of care neoadjuvant chemotherapy regimen containing both an anthracycline and a taxane. Following treatment, the patient's clinical outcome was evaluated (see Patient Outcome Evaluation).

Patient Outcome Evaluation. Patient treatment response was determined after completing neoadjuvant chemotherapy. Resection specimens were analyzed for pCR (yes / no). In addition, patient treatment outcome was measured based on the CPS+EG score [78]. All patient treatment outcomes were determined by a pathologist.

Magnetic Resonance Imaging. Patients had pre-treatment and post-treatment gadolinium dynamic contrast-enhanced magnetic resonance imaging (MRI) on 3T MRI which was used as an imaging additional method to determine tumor and breast tissue perfusion. Scans were taken pre-contrast, and post contrast at 90 seconds, 3.5 minutes, and 5.5 minutes. Patients with MRIs not conforming to this criteria were excluded from the MRI Analysis.

MRI Analysis. Analysis of MRI data was performed using OsiriX DCE Tool Plugin [97]. Area under the curve was measured using a 3D spherical ROI over the tumor region determined by a radiologist, and the hotspot (maximum signal in a 1 cm^3 region given the original ROI) was measured for the tumor. A control ROI the same size as the tumor ROI was used on the contralateral breast, in the same general anatomical position as the tumor and used for normalization, as this is considered to be a baseline for the individual patient's normal tissue vasculature. See Supplementary **Figure 2.7** for MRI image examples and analyses performed.

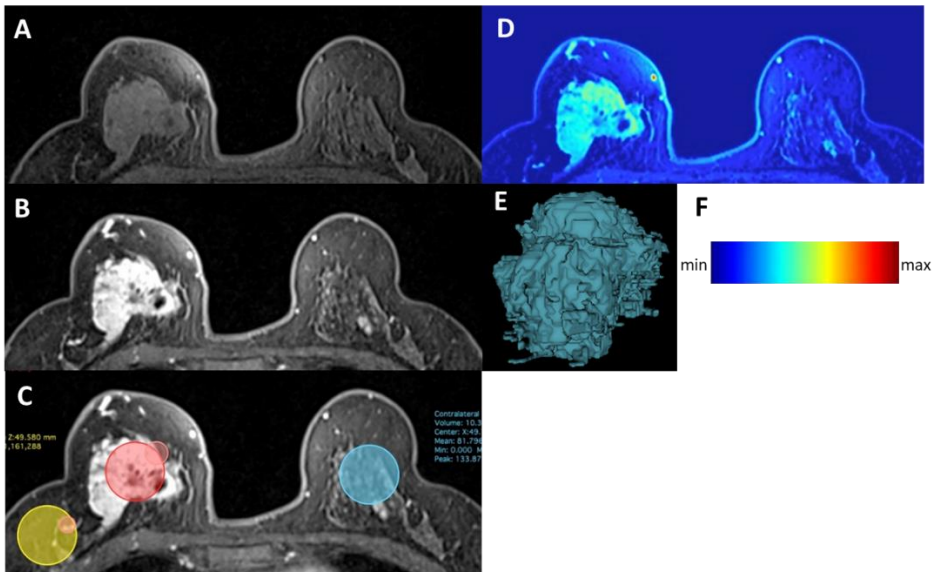

Figure 2.7. Dynamic contrast-enhanced magnetic resonance imaging axial view. **A)** Before contrast agent was injected, **B)** 90s post-contrast, **C)** 90s post-contrast with regions of interest (ROI) colored in red (tumor), yellow (normal tissue on isolateral breast), blue (normal tissue on contralateral breast). Note the smaller orange ROIs associated with the red and yellow ROI, these are $1cm^3$ "hot spots" (maximum signal given the original ROI) **D)** area under the curve map, analysis in Figure 2.5 was obtained from this map with the ROIs shown in C **E)** Tumor ROI shown in 3D view, **F)** area under the curve map signal intensity scale.

Histology. Patient tissue samples were formalin-fixed and paraffin embedded, and processed per institutional standard of care, in compliance with ASCO-CAP guidelines. The Human Tissue Repository and Tissue Analysis Shared Resource at the University of New Mexico's Cancer Center served as an honest broker for access to all tumor specimen. CD34 antibody staining via immunohistochemistry was used to highlight tumor vasculature. Additionally, hematoxylin and eosin stain was performed to evaluate tissue morphology (e.g. tumor, non-tumor)

Histology Semi-automated Analysis. Patient histological samples from patients Cohort A, and patient core biopsy samples from patients Cohort B were analyzed using HALO image analysis software (Indica Labs) to separate out tissue regions from the CD34 stained tissue sections: $CD34^+$ tissue regions (vasculature), $CD34^-$ tissue regions (non-vasculature tissue), and background regions (non-tissue). HALO uses machine learning to classify tissue regions based on a training set. Tissue regions were separated into 1x1 mm^2 square regions for analysis using code developed in Matlab (MathWorks). The code developed takes the separated regions

(separated by HALO) and measures vasculature radius, r_b (µm), measured along the short axis of the vessel; short axis is used due to the consideration that the vessel could be in the plane of the tissue section. See **Figure 2.8** for outline of analysis. Multiple measurements were taken for each vessel to get an accurate measurement of radius for each vessel with an average taken for an r_b value for each grid analyzed. The blood volume fraction, BVF, was taken to be the vasculature area (in red) divided by the whole tissue region (blue + red in **Figure 2.8C**). Only tissue regions were considered for BVF measurement. From the perimeter of each vessel, the maximum distance drug/blood/nutrients would have to diffuse to feed the whole tissue region is calculated and shown at each point in black. All distances to nearest vessel (in red) are taken and averaged for each grid analyzed to get the diffusion penetration distance, *L*, measured in µm.

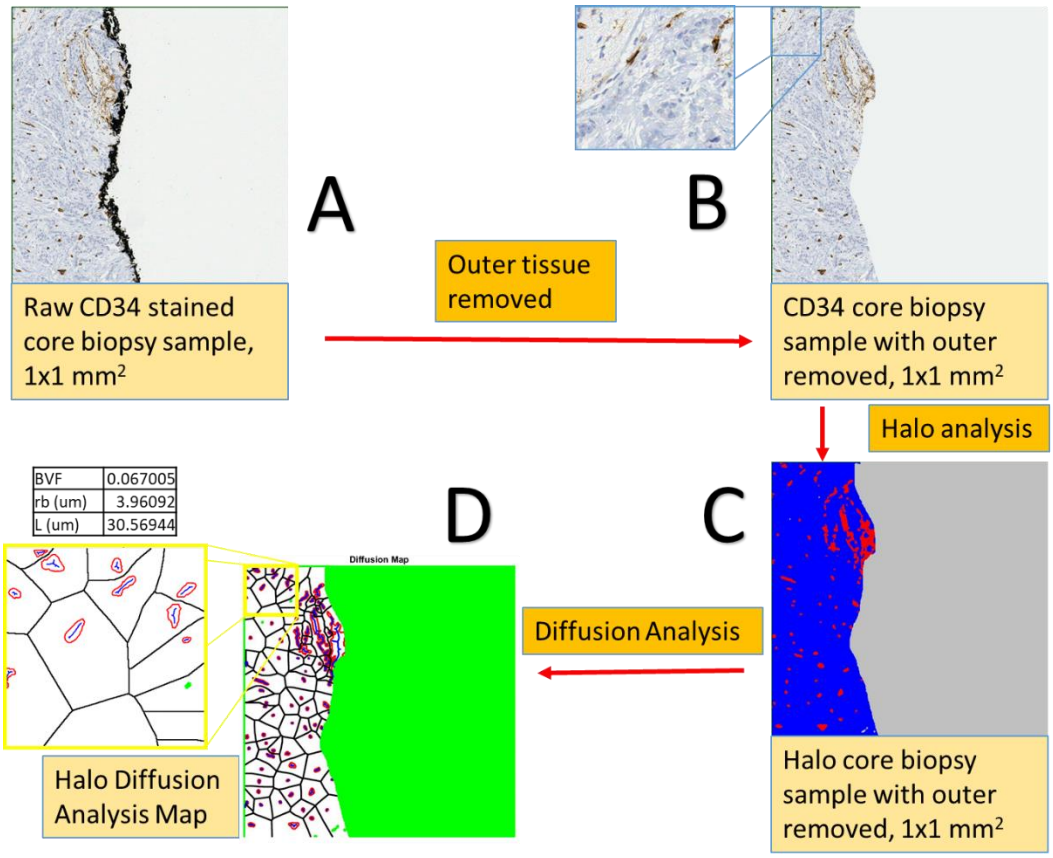

Figure 2.8 Diffusion analysis schematic. A) Shows the original CD34 stained histology grid before any processing. **B)** Displays the same tissue region as in A, but with the outer inked portion removed due to the increased likelihood of false positives on the perimeter of core biopsy samples (the pathology department inks tissue cores for quality purposes). **C)** Demonstrates a computerized version of B and differentiates between tissue $CD34^-$ (blue), vasculature $CD34^+$ (red), and non-tissue regions (grey). **D)** Shows the diffusion analysis of image C, which was performed by code developed in Matlab. Average measurements taken for the image are: vessel radius (r_b), blood volume fraction (BVF), and diffusion distance (L). Vessels are outlined in red, and total area of blood vessels in a tissue region is blood volume fraction, BVF. Radius of blood vessels which are measured at each blue point inside of a vessel (outlined in

red). An average of all vessel radii in each image analyzed is taken to be r_b (μm). The farthest distance nutrients or drug need to travel from a vessel to reach all tissue, the distance from that point to vessel in red is measured at each point in black, all distances averaged is the diffusion penetration distance, *L*, measured in μm. White is the tumor tissue region, all of which is considered for analysis. Green is the background/non-tissue region not considered for analysis.

Mathematical Model.

$$f_{kill} = 2 \cdot \mathrm{BVF} \cdot \frac{\sqrt{\mathrm{BVF}} \cdot K_1(r_b/L) - K_1(r_b/(L \cdot \sqrt{\mathrm{BVF}}))}{\sqrt{\mathrm{BVF}} \cdot r_b / L \cdot K_0(r_b/L) \cdot (1 - \mathrm{BVF})} \quad \textbf{[Eq. 2.2]}$$

f_{kill} equation with parameters r_b, BVF, and *L*, which are directly measured from histology semi-automated analysis. f_{kill} is the fraction of tumor cells killed in a patient predicted as a function of the other parameters on the right side of the equation. r_b is the average radius of blood vessels in the tissue section analyzed. BVF is the fraction of blood volume in the tumor. *L* is the farthest distance nutrients/drug need to travel from a vessel to reach all tissue [86].

Statistics Analysis and Graphing. Matlab and GraphPad Prism 7 were used to determine best fit using patient averages for BVF, r_b and *L* placed into Eq. 2.2 and using non-linear regression solving for L/r_b ratio. Fits were obtained using initial values for fit, $L/r_b = 20$ and $L/r_b > 0.005$ for a constraint.

CHAPTER 3

NANOPARTICLE UPTAKE AND CANCER TREATMENT EFFICACY MODELING

This chapter was adapted from:

Brocato, T.; Coker, E. N.; Durfee, P. N.; Lin, Y. S.; Townson, J.; Wyckoff, E. F.; Cristini V.; Wang, Z. Understanding the Connection between Nanoparticle Uptake and Cancer Treatment Efficacy using Mathematical Modeling. Submitted to *Nanomedicine: Nanotechnology, Biology and Medicine*.

3.1 Overview

Cancer represents the 2nd major cause of death in the United States, and one out of eight women is estimated to develop invasive breast cancer in her lifetime [98]. Breast cancer tumors are heterogeneous, and the series of events which cause them to grow, shrink, or metastasize are complex, involving interactions with and influences from their microenvironment [99]. It is known that the heterogeneity of the breast cancer tumor greatly complicates our understanding of the disease and the development of effective treatment [99]. In fact, most tumors are heterogeneous both phenotypically and functionally [100], resulting in variable traits among different tumors. Understanding an individual's response based on these differing traits is essential for predicting and improving patient-specific treatment response.

Due to drug toxicity and non-specificity, a spectrum of different particles have been developed for both particle-based drug delivery and for imaging of particle distribution, including superparamagnetic iron oxide nanoparticles [101], lipid bilayer encapsulated nanoporous silicon or mesoporous silica particles for drug/cargo delivery [102-104], and silica based nanoparticles [105], to name a few. Here, we discuss the use of mesoporous silica nanoparticles (MSNPs), which possess the benefits of a high cargo capacity, due to their immense internal surface area (800-1000 m^2/g), facile surface modification to enable targeting, low toxicity, therapeutic effectiveness [106, 107], and increased circulation time, therefore increasing total tumor drug uptake [107]. As a result, the effective therapeutic drug dosage is reduced when delivered using MSNPs relative to the free drug delivery case, minimizing treatment side effects.

Using an integrated mathematical modeling and experimental approach, our group has shown that nanocarrier mediated drug delivery of doxorubicin achieves equal cell kill efficacy at a dose only 20% of that of the corresponding free doxorubicin in a hepatocellular carcinoma cell model *in vitro*. In the present study, we use 50-nm diameter acetylated MSNPs, modified with polyethylene glycol (PEG) and polyethyleneimine (PEI) as first reported in Townson et al.[103] These acetylated MSNPs were found to be colloidally stable and non-toxic. They were shown to have reduced non-specific binding to cell types A549, A431, Hep3b and hepatocytes *in vitro*, as well as to endothelium and white blood cells, and were observed to remain in circulation over 6 hours post injection in a chorioallantoic membrane (chicken embryo) model [103]. The increased circulation time of the acetylated MSNPs (> 6hrs) greatly improves their likelihood of entering the tumor and delivering effective drug dosages to cancer cells when compared to the circulation time of free drug (<2 hrs, $t_{1/2}$ = 1.68 hrs) [6].

A number of techniques have been developed to monitor the pharmacokinetics and biodistribution of nanoparticles in living animals, including optical fluorescent microscopy imaging [108-110], ultrasound [111], in vivo bioluminescence (IVIS® using luciferase) [112-114], and PET, SPECT, and CT (as well as combinations of these techniques) using appropriate contrast agents [108, 109, 115-117]. However, successful prediction of treatment outcome based solely on parameters measured from the biodistribution of nanoparticles is challenging because the distribution of nanoparticles and of drug are different and heterogeneous across tissues, organs, and even whole organisms. We have previously developed a mathematical model[72, 118] that predicts the fraction of tumor killed by chemotherapeutic treatment (denoted by f_{kill}) based on drug uptake and nanoparticle drug flux. f_{kill} was shown to be quadratic with respect to time, especially in the

initial phase of a treatment. In the present study, we seek to expand upon this model[72, 118] in order to develop a mathematical theory to predict nanoparticle-based treatment efficacy based on quantitative data obtained from measured nanoparticle biodistribution.

Measurement of drug distribution *in vivo* is often difficult and expensive. Typically, quantitative analysis of nanoparticle biodistribution is done through organ dissection after injection of labeled nanoparticles, followed by imaging, using methods such as transmission electron microscopy or optical microscopy, or by elemental analysis using inductively coupled plasma-atomic emission [119]. Nanoparticle distribution can also be measured *in vivo* using magnetic resonance imaging and magnetic particle imaging [119]. Here, capitalizing on the low natural abundance of elemental silicon in mammals, we performed Si elemental analysis of the major organs in order to measure MSNP concentrations, and then compared these quantified MSNP accumulation values to changes in tumor volume. By using our theory to link measured tumor growth with nanoparticle distribution and concentration, and considering the effects of vasculature and diffusion characteristics, we were able to successfully predict the *in vivo* therapeutic efficacy of MSNP-delivered doxorubicin to 4T1 breast cancer tumors in mice.

3.2 Results and Discussion

Cancer stage at the time of diagnosis is demonstrated to be an important predictor of morbidity and survival [120]. Five-year survival rates for breast cancer are 99% when diagnosed pre-metastasis, but with a significant reduction to only 25% five-year survival rate when the tumor has metastatized [120]. In order to better understand the difficulties of effective theraputic

treatment when patients are diagnosed at a later stage, our experiments focused on treating tumors that were relatively large with distant metastases prior to the start of a treament. Accordingly, we implemented a 4T1 cell line experiment in BALB/c mice, in order to study stage IV human breast cancer with metastasis in the presence of an active immune system.

Treatment efficacy between MSNPs loaded with doxorubicin (Dox) and free Dox was compared at the same dosage; phosphate buffered saline (PBS) was used as a control in a third treatment group. Tumor size measurements in mm^3 are shown in Figure 3.1 for three groups of seven mice each treated using PBS (control), free Dox, or MSNPs loaded with Dox. Due to this treatment being adminstered at a later stage of breast cancer, it can be observed that free Dox treatment is not effective at a late stage; but the nanoparticle treatment shows some efficacy. This late stage study confirms that MSNPs loaded with Dox exhibit a better treatment outcome than the other treatment groups, indicating Dox loaded MSNPs are more effective than Dox administered alone.

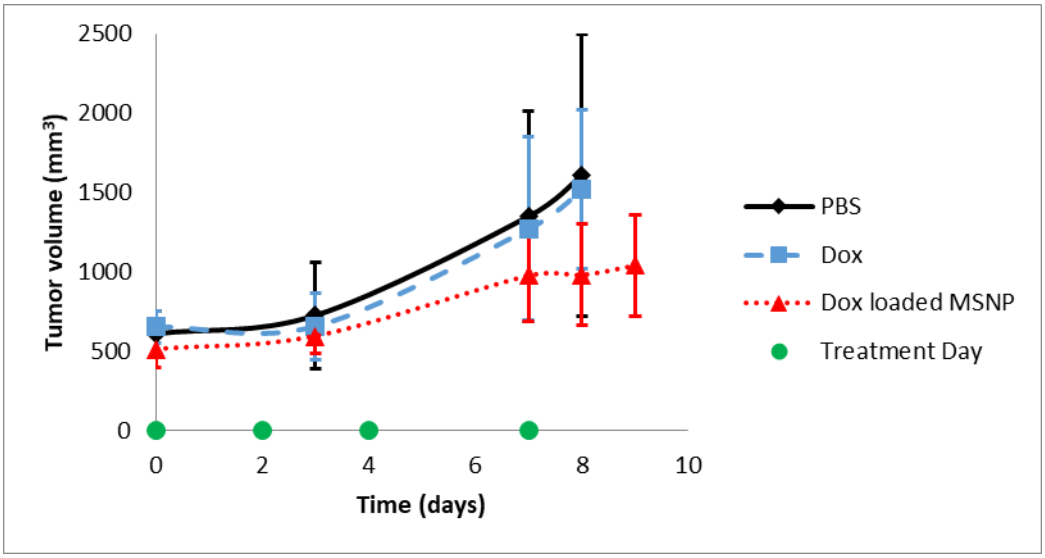

Figure 3.1. Average tumor volume measurements. Three treatment groups (7 mice/group): PBS (control), free doxorubicin (Dox), and 50nm MSNPs loaded with Dox. Each group's average tumor size is shown above. Measurements were taken on days 0, 3, 7, 8, and 9. Treatments were given on days 0, 2, 4, and 7.

In vivo biodistribution of nanoparticles based on size, shape, composition, and surface characteristics is still not well understood, as are the details of nanoparticle removal from circulation by the reticuloendothelial system [121]. To gain a better understanting of these important parameters, we used graphite furnace atomic absorption (GFAA) to measure silicon (Si) concentration and distribution within tissues of interest [122]. The Si concentration in the control (PBS) group was used as a baseline for the background Si concentration which occurs naturally in tissues (Si has important biofunctionality, and thus is found in trace quantities in many tissues). As expected, we observed that the amount of naturally occurring Si in the control tissues was low relative to the signal of MSNP in treated tissues (Figure 3.2, control). Figure 3.2 shows measured values of elemental Si determined by GFAA, presented as the mass percentage of Si in the corresponding tissue being tested in mouse organs from the control and Dox loaded MSNP treatment groups after 9 days of treatment and sacrifice. The tissues tested were tumor, kidney, liver, spleen, as well as a measured sum of all organs. The sum of all organs tested corresponded to ~2–4.4% of the total injected Si dose, as shown in supplementary Figure 3.4.

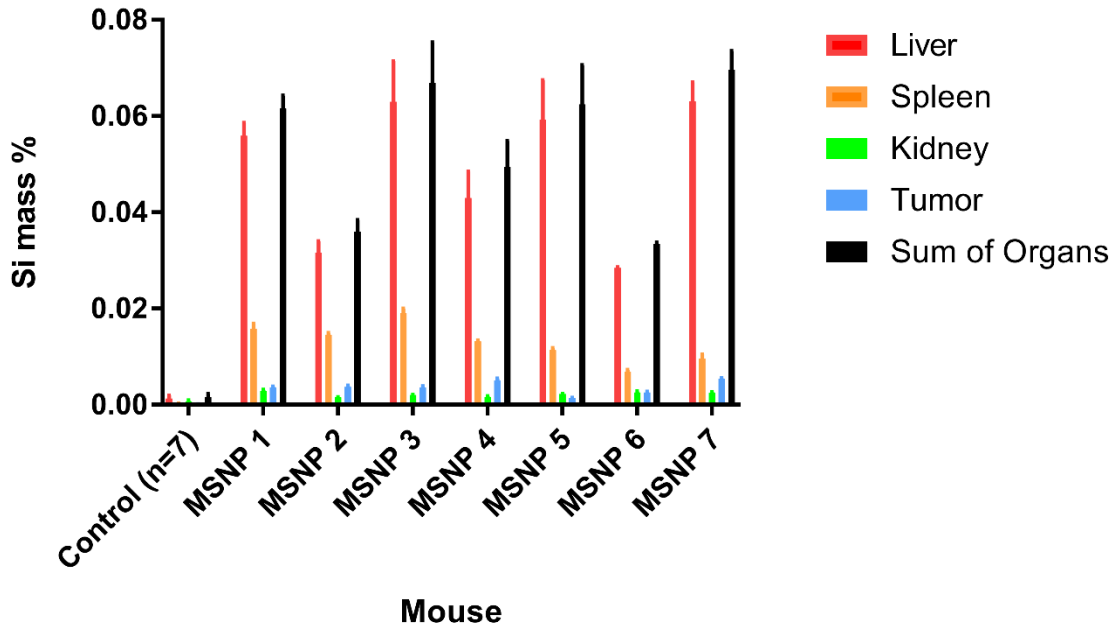

Figure 3.2. MSNP deposition (Si mass %) in liver, spleen, kidneys, tumor, sum of organs, and average Si concentration naturally in tissues (control group) taken post-sacrifice (day 9). Data were obtained using GFAA spectrophotometry. Error bars are calculated based on the standard additions method used to calculate Si concentrations.

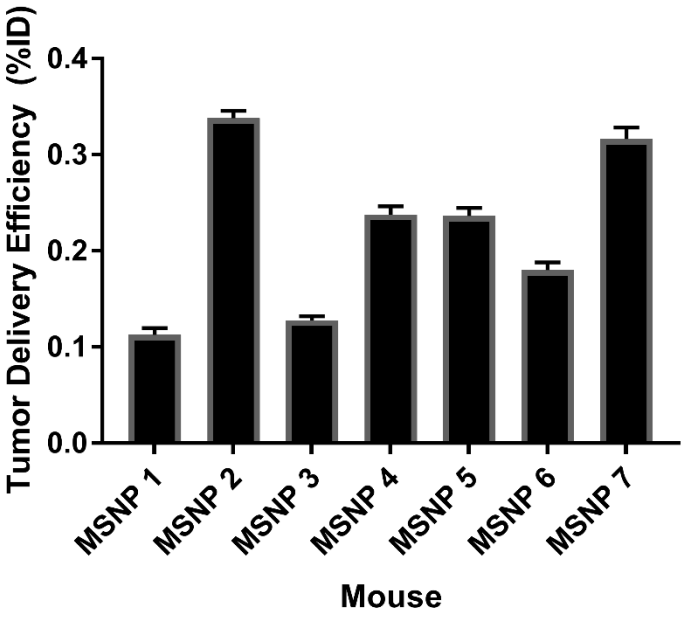

Figure 3.3. Tumor delivery efficiency (%ID). Data were obtained using GFAA spectroscopy. Absolute Si mass % in tumor was subtracted from naturally occurring Si measured by testing control tumors in mice not exposed to MSNPs. Delivery efficiency is Si mass % in each tumor multiplied by tumor volume.

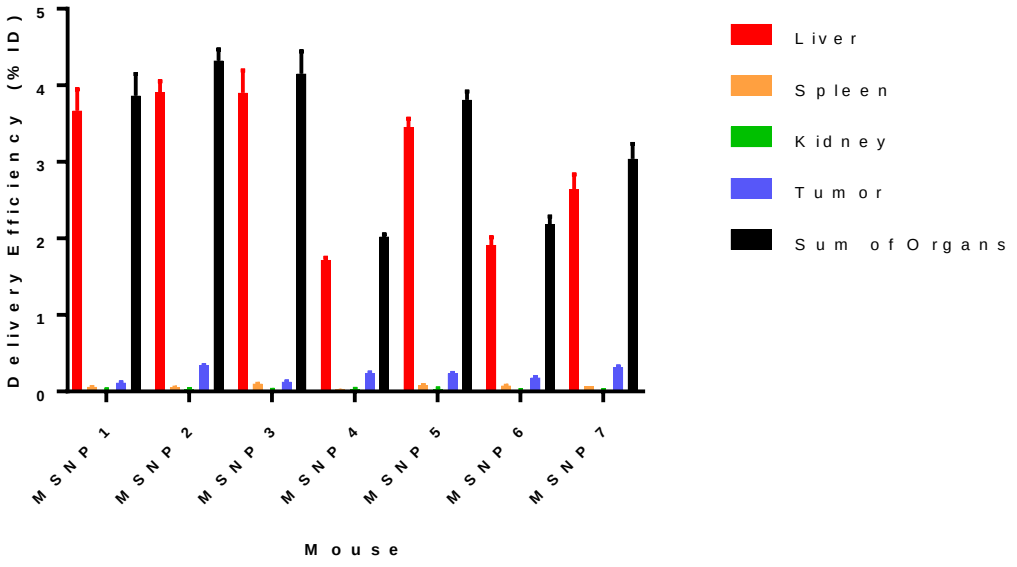

Figure 3.4. Delivery efficiency (%ID) in liver, spleen, kidneys, tumor, and sum of organs. Data were obtained using GFAA spectroscopy. Absolute Si mass % in organs were subtracted from naturally occuring Si measured by testing control mice not exposed to MSNPs.

Mice, even within the same treatment group, demonstrated a wide range of f_{kill} responses, indicated by the large standard deviation seen in tumor volumes in Figure 3.1 (error bars). Moreover, the concentrations of Si deposited in the liver, spleen, kidney, and tumor were shown to vary without correlation between uptake in the tissues measured (Figure 3.2). For example, mice that had greater MSNP uptake in the liver did not have greater or lesser uptake in the tumor, see Figure 3.3 for tumor delivery efficiency (%ID), and mice with less MSNP uptake in the tumor did not have less or more uptake in other organs. From our experiments here, we find that the MSNP delivery efficiency to the tumor is about 0.22%ID on average. Based on an extensive review of papers over the past ten years, Wilhelm et al reports 0.7%ID as being the average tumor delivery efficacy using a multitude of particles, cancer types, and measurement methods, and mentions that, "it is possible that the amount of nanoparticles reaching cancer cells and their subcellular compartments in vivo is much less than 0.7%ID because nanoparticles need to cross the tumour extracellular matrix to reach the cancer cells."[123] Hence, our data seems well consistent with Welhelm et al's paper. One paper used elemental analysis, ICP-AES, to measure silica nanoparticle concentration, of which the %ID was determined to be 0.29, 1.6, and 10.8%ID[124], most of the quantifications used to calculate the average of 0.7%ID in a tumor used PET scans as a method of quantification [110, 116, 125, 126]. Thus, the biodistribution of nanoparticles was observed to show significant variability, even amongst

similar mice under the same treatment protocol. Blood volume fraction (i.e., the volume of the tumor occupied by blood vessels) was previously shown to be an important factor in predicting f_{kill} in human colorectal cancer metastasized to the liver [86].

Many current nanoparticles have achieved the capability to release drugs at a nearly constant, sustained rate for a period of days, weeks, or even months [127-129], although this rate may be dependent on other physiochemical properties of the particles, such as the surface chemistry and pore size [130]. *In vivo*, this nearly constant drug release rate results in an approximately unchanged rate of change of drug flux (denoted by F) across blood vessels. By further assuming a linear drug uptake by cancer cells, we have devleoped a special form of f_{kill} for predicting treatment efficacy for nanoparticle-based drug delivery systgems [118]. We found that tumor response *in vivo* to Dox loaded nanoparticles occurs quadratically over time, at least for the first several days (Eq. 3.4; also see Methods), and have further validated this model using experiments on a breast cancer mouse model. Accordingly, we used this quadratic tumor response model to link the MSNP deposition with measured changes in tumor volume (relative to control). The quadratic tumor response coefficient (i.e., f_{kill} coefficient: Θ_f) was determined to have an exponential relationship with MSNP deposition in the tumor tissue (Figure 3.5). Θ_f was found to be predictable based on tumor silicon content with 95% confidence ($R^2 = 0.817$, $p_{.05} = 0.0007$). This indicates that increasing chemotherapy drug delivery, using a MSNP transport vector, results in an exponentially greater rate of tumor kill. Values for comparison are shown in Table 1, along with statistics that indicate that most model values are statistically significant at 95% confidence except for MSNP 5. MSNP 4 and 7 did not show measurable response to treatment until day 7, resulting in only two data points; therefore, p-values for Θ_f could not be

determined due to an insufficient number of points. As such, these two mice were removed from further analysis. Together, this indicates that MSNP uptake is an important factor in determining tumor treatment efficacy. However, more tumor measurements and/or a longer experiment would be beneficial to validate statistical significance with the model predictions.

Table 3.1. Tumor f_{kill} coefficients (Θ_f), as described by Eq. 3.4, show a similar order to Si deposition values. The Si deposition values are also shown in Figure 3.2 (MSNP deposition) and in Figure 3.5 (R^2, Θ_f, t_0), showing the exponential relation to the tumor f_{kill} coefficient calculated using Eq. 3.4.

Mouse	Si % in tumor	t_0 (time tumor begins to respond to treatment in days)	Θ_f (quadratic response coefficient)	p-value	R^2 (quadratic)
MSNP 4	0.00513	-	0.4621	-	-
MSNP 7	0.00535	-	0.3068	-	-
MSNP 2	0.00372	0	0.0096	0.0030	0.9648
MSNP 3	0.00362	0	0.0067	0.0050	0.9499
MSNP 1	0.00360	0	0.0064	0.0110	0.9155
MSNP 5	0.00138	0	0.0027	0.1990	0.4728
MSNP 6	0.00260	0	0.0013	0.0060	0.9409

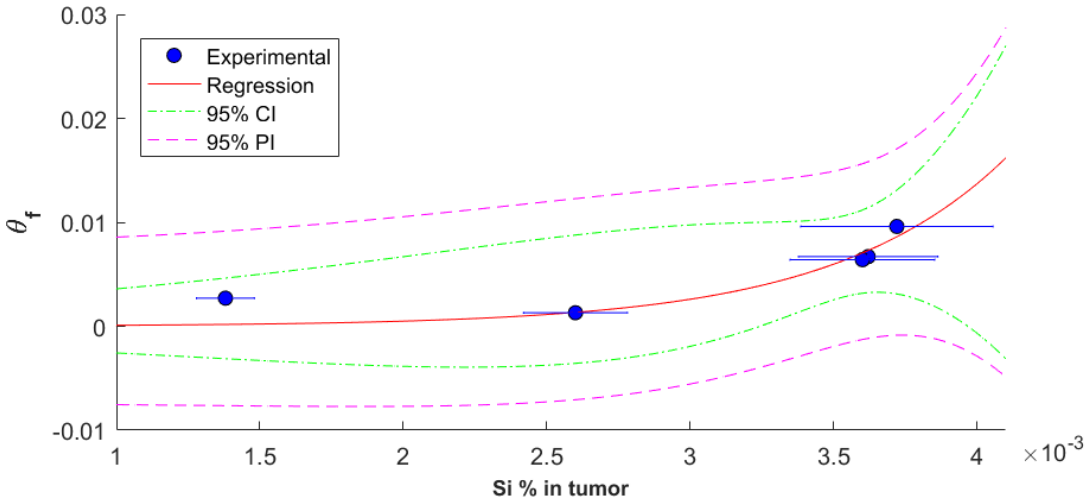

Figure 3.5. Si concentration and f_{kill} coefficient (Θ_f) determination. Θ_f, explained in Eq. 3.4, is predicted based on tumor Si absolute mass percentage in tumor, as measured using graphite furnace atomic absorption (GFAA). R^2 = 0.817, $p_{.05}$ = 0.0007 for quadratic f_{kill} coefficients calculated after 9 days of treatment and sacrifice. This was determined by the best fit between f_{kill} and Si concentration using an exponential fit (which represents the best fitting function among many we have tested, including linear and nonlinear functions, e.g., the Hill function). Experimental mouse tumor f_{kill} was determined using Eq. 3.2 for mice treated with MSNPs. Model mouse tumor f_{kill} was determined by optimizing values for t_0 (days in integer values), described in Eq. 3.4.

We then performed correlation analysis to compare model results (computed as $f_{kill} = 0.000172 \cdot e^{1664.39 \cdot Si} \cdot t^2$, where *Si* is tumor Si mass %) and the corresponding time course MSNP experimental data, as shown in Figure 3.1. We obtained correlation coefficient r = 0.89 and p < 0.001, and thus consider the model to be acceptable in predicting MSNP-based treatment outcome with absolute Si mass percent as input.

Cancer treatment can be improved greatly by using MSNPs as chemotherapy delivery vessels, which allow for an increased effective drug dose to be delivered to the tumor site due to drug sequestration within the particles during transit to the site, resulting in reduced uptake by the reticuloendothelial system and longer circulation time [131]. We have provided further insight into this drug delivery system using MSNPs in a murine 4T1 *in vivo* tumor model combined with a mathematical modeling description of drug efficacy. In particular, our mathematical model demonstrates that an increase in MSNPs delivered to the tumor exponentially increases the cell kill at early times in the treatment, leading to improvements in overall treatment outcome. The major hurdle is thus increasing tumor MSNP delivery over current methods, as any increase in delivery to the tumor is expected to significantly improve treatment efficiency. In this perspective, active tumor targeted delivery of chemotherapy via targeting ligand modified nanoparticles[102, 132] is expected to enhance treatment efficacy.

Morover, if the quadratic f_{kill} coefficient could be determined early on, the treatment efficacy could be predicted by our mathematical model. It has been demonstrated that tumor exponential growth rate constants were correlated to patient survival [133]. Here, we demonstate that, due to external stresses and regression in tumor size due to treatment, the quadratic coefficient following treatment is predictive of treatment uptake and therefore treatment efficacy. Note that Θ_f is a combination of parameters, inlcuding drug flux across blood vessels, cell death due to accumulated drug, and initial tumor volume (see [118] for details). This implies that Θ_f may have a nonlinear relationshiop with Si content, which has been confirmed in this study where an exponetial relation was found. In future efforts, a better understanding of nanoparticle biodistribution behavior will allow us to have a more adaptive use of the model

presented here. Additionally, further model validation against information obtained from non-invasive imaging modalities such as MRI, PET/CT [134] will help to quantify nanoparticle-based treatment outcome without the need to sacrifice animals. This important next step will also progress the model towards a more clinical functionality, where it may be implemented as a predictive tool without the need for invasive diagnostic procedures.

3.3 Materials and Methods

Mathematical modeling. We recently developed a series of mathematical models in closed form for predicting tumor response to treatment based on time- and space-dependent drug diffusion and perfusion properties [61, 72, 86, 88, 89, 91, 118]. A generalized model presented in [118] can provide predictions of outcome for both conventional chemotherapy with a specific dosing and timing regimen and nanoparticle-based treatment. f_{kill} (i.e., the fraction of tumor killed by treatment) is defined as:

$$f_{\text{kill}} = 1 - \frac{V_i(t)}{V_{\text{C}}(t)}, \qquad \text{(Eq. 3.1)}$$

where V is tumor volume at time t, i indicates drug treatment group, and C indicates the control group. Normalizing tumor volume at a given time t to initial volume, we have

$$f_{\text{kill}} = 1 - \frac{V_i(t)/V_i(t_0)}{V_{\text{C}}(t)/V_{\text{C}}(t_0)}, \qquad \text{(Eq. 3.2)}$$

where t_0 is determined to be the initial day when treatment was started; in our analysis here, i simply indicates either free DOX or MSNP treatment group.

Assuming that drug-loaded nanoparticles can accumulate within tumors and continuously release drugs at a nearly constant rate over a certain time interval (especially at the initial phase of a treatment), we derived a special form of f_{kill} [118]:

$$f_{kill} = \frac{F \cdot \lambda_k}{2V_{T,0}} t^2, \qquad \text{(Eq. 3.3)}$$

where F is the flux of drug across blood vessel walls, λ_k is the death rate of tumor cells, $V_{T,0}$ is the tumor volume when tumor begins to respond to treatment (positive f_{kill}), and t is time. Note that there is another key assumption we made to the original f_{kill} model, which is composed of a system of differential equations, in order to develop this simplified form: a drug administered as bolus at a certain dose level has the same effect as the same total amount of drug administered over several months at a constant, smaller dose level [91]. That is, this model functions for a number of situations, including (1) single drug injection at the beginning, (2) multiple drug injections over the course of treatment, and (3) continuous drug administration. Regardless of how we administer the drug, the treatment system can be modeled as a continuous drug delivery system. This assumption has been validated previously *in vivo* and in patients across different types of cancer [86, 118].

Parameters for best model fits to experimental data (determined by Eq. 2) with the model's predictions from Eq. 3 are derived from:

$$f_{kill} = \theta_f \cdot t^2, \qquad \text{(Eq. 3.4)}$$

where Θ_f is the tumor f_{kill} coefficient ($\Theta_f = \frac{F \cdot \lambda_k}{2V_{T,0}}$). From our experimental analysis, we obtain:

$$\theta_f = A \cdot e^{B \cdot Si}, \qquad \text{(Eq. 3.5)}$$

where coefficients *A* and *B* are fit to determine best values for prediction between Si absolute mass percentage and the model output, Θ_f. *A* and *B* are tumor and drug specific coefficients specific to 4T1 breast cancer given treatment when tumors are ~500mm^3 when beginning treatment. *A* and *B* are the same for all 5 mice given the treatment described under the experimental description used to describe the relationship between Si mass % deposited in 4T1 breast tumors and Θ_f, shown in Figure 3.5.

Experiment description. Mouse experiments were performed using protocol approved by the UNM Office of Animal Care Compliance. Six- to eight-week-old female BALB/c female mice were given subcutaneous injections of 5×10^5 4T1 (ATCC® CRL2539™) cells into the right flank. Tumors were grown for two weeks before treatment initiation. Average tumor volumes, calculated from diameters measured externally with calipers, are shown in Figure 3.1. Mice were randomly divided into three treatment groups (7 mice/group, 21 mice total): control (PBS), free doxorubicin 1mg/kg per treatment, 1mg acetylated MSNPs (50 nm, 2.5 nm pores) loaded with doxorubicin (equivalent 1mg/kg doxorubicin per treatment). Acetylated MSNPs were made using the protocol described in Townson et al[103], and loaded with doxorubicin using the drug loading protocol for water soluble doxorubicin in Lin et al.[135] Treatment was given starting 2 weeks after tumor cell injections. Treatment days were as follows (t = 0 is 2 weeks following tumor injection): 0, 2, 4, and 7. All mice were sacrificed on day 9. Tumor measurements were taken on days: 0, 3, 7, 8, and 9. Tissues were excised and fixed in 4% formaldehyde diluted in PBS, and then Si contents were determined using graphite furnace

atomic absorption spectrometry as described below. Statistical analysis was conducted using Matlab, Excel, and Graphpad Prism.

Graphite Furnace Atomic Absorption Spectrophotometry (GFAA). Analysis of Si concentration in MSNP (mesoporous silica nanoparticle) and control (PBS) treated mice tissue was tested using a THGA graphite furnace on a PinAAcle 900T Atomic Absorption Spectrophotometer (Perkin Elmer, USA. Tissues tested were tumor, kidney, spleen, and liver digested using tetramethylammonium hydroxide. Si absolute mass percentages in tissues were measured using the standard additions method, commonly used for samples with a matrix that alters the signal when different matrix concentrations of sample are tested. Tumor (or organ too depending on Figure 3.2 chosen) delivery efficiency, %ID, was determined by using BALB/c standard organ values from Tsai et al to estimate total organ Si mass deposited [136]. Total Si delivered was calculated based on Si percentage (39.36% of nanoparticle mass) added during synthesis using the protocol in Townson el al [103]. Tumor delivery efficiency was determined using Si absolute mass percentage in the average control mice each respective organ subtracted from that of the MSNP treated mouse and dividing it by the total administered dose over the treatment duration. See Supplementary Information for more details on GFAA methods.

CHAPTER 4

CONCLUSIONS AND FUTURE DIRECTIONS

This chapter was adapted in part from from:

Brocato, T.*; Dogra, P.*; Koay, E. J.; Day, A.; Chuang, Y.; Wang, Z.; Cristini, V. Understanding Drug Resistance in Breast Cancer with Mathematical Oncology. Current Breast Cancer Reports, 2014. 6(2): p. 110-120. (*Authors contributed equally to this work)

And in part from:

Brocato, T.; Coker, E. N.; Durfee, P. N.; Lin, Y. S.; Townson, J.; Wyckoff, E. F.; Cristini V.; Wang, Z. Understanding the Connection between Nanoparticle Uptake and Cancer Treatment Efficacy using Mathematical Modeling. Submitted to *Nanomedicine: Nanotechnology, Biology and Medicine*.

And in part from:

Brocato, T.*; Glaberman-Brown, U.*; Wang, Z.*; Selwyn, R.; Wilson, C. M.; Wyckoff, E. F.; Lomo, L.; Saline, J.; Pasqualini, R.; Arap, W.; Brinker, C. J.; Cristini, V. Mathematical Modeling to Predict Response to Neoadjuvant Chemotherapy Using Breast Cancer Vasculature Characteristics. Submitted to *Science Advances*. (*Authors contributed equally to this work)

4.1 Mathematical Modeling of Chemotherapy

Chemotherapy is the mainstay of treatment for the majority of patients with breast cancer but results in only 26% of patients with distant metastasis living 5 years past treatment in the United States, largely because of drug resistance. The complexity of drug resistance calls for an integrated approach of mathematical modeling and experimental investigation to develop quantitative tools that reveal insights into drug resistance mechanisms, predict chemotherapy efficacy, and identify novel treatment approaches. A review has been done in Chapter 1 of recent modeling work for understanding cancer drug resistance through the use of computer simulations of molecular signaling networks and cancerous tissues, with a particular focus on breast cancer. These mathematical models are developed by drawing on current advances in molecular biology, physical characterization of tumors, and emerging drug delivery methods (e.g., nanotherapeutics). The review focused on representative modeling works that have provided quantitative insight into chemotherapy resistance in breast cancer and how drug resistance can be overcome or minimized to optimize chemotherapy treatment.

4.2 Multiscale Modeling and Treatment Drug Resistance

Cancer results from multiple genetic, epigenetic, and environmental factors in a developmental context across a number of biological scales in time and space.[10] Hence, understanding cancer drug resistance mechanisms by mathematical modeling should not be limited to any specific biological scale, whether it is at the molecular level (gene, protein, or signaling network) or higher, such as a tissue or organ level. By integrating data from multiple

levels of biological complexity, modeling tumor resistance to chemotherapy drugs across different scales can potentially be more powerful in guiding the development of new treatment strategies. In this perspective, by taking into account important oncological characteristics such as individual and collective cellular activities, tumor heterogeneity, and the changing heterogeneous microenvironment, a multiscale model of drug resistance may provide a new means of predicting the overall tumor drug resistance behavior in responding to changes that occur on any biological scale. This research has not yet been fully explored in the field. It is also noteworthy that the development of a successful cancer model of drug resistance is a long-term process, and that available experimental data should be used to guide the model design and to verify and validate model results.

4.3 Diffusion Barriers Model- Neoadjuvant Treatment Prediction based on Biomarkers

Breast cancer is a model disease for the development of both targeted therapy and prognostic and predictive biomarkers. However, predictive biomarker based treatment selection remains an elusive goal in the management of many women with this disease. A modeling tool was presented to predict the likelihood of response to neoadjuvant chemotherapy using patient specific tumor vasculature biomarkers. A semi-automated analysis was implemented to allow for increased measurement accuracy and rapid throughput in rendering model predictions, with 3990 images, 10-208 images analyzed for each patient, in a total of 48 patients. A previously developed histology-based model was applied to primary resected breast cancer tumors. In effort to translate this model towards clinical practice, prospective and a retrospective cohort of patients undergoing neoadjuvant chemotherapy were evaluated, collecting clinically relevant data including pre- and post-treatment pathology

specimens, and dynamic contrast-enhanced magnetic resonance imaging. Additionally response was correlated to neoadjuvant chemotherapy with the pretreatment tumor vasculature biomarkers and model parameters. Analysis of histology parameters, specifically radius of drug source divided by diffusion penetration distance (L/r_b), a normalization penetration distance, and blood volume fraction (BVF), provides a separation of patients obtaining a pathologic complete response (pCR) and those that do not, with 80% accuracy (p= 0.0269). This diffusion barriers model has the potential to serve as predictive biomarker in the neoadjuvant setting, thereby allowing a personalized approach to breast cancer treatment.

4.4 Future Directions

In an effort to push this research forward patient histology analysis automation has been explored with significant findings, additionally with a non-invasive tool (MRI) to grab the same parameters, demonstrating the importance of vasculature normality in the tumor tissue. These parameters indicate the importance of obtaining a normal vasculature network throughout the tumor to deliver chemotherapeutic agents. Additionally in Chapter 3, the importance of delivering a large concentration of nanotherapeutics was demonstrated in order to achieve exponentially greater response to treatment. The combination of mathematical modeling to understand patient vasculature biomarkers, measured through histology and MRI, and the importance of increasing the delivery of treatment agents to exponentially increase treatment outcome, greatly benefits the understanding of cancer treatment outcome and direction we need to head in. The next step would be go use this semi-automated analysis to analyze vasculature parameters in conjunction with nanotherapeutics and their clinical outcome. Nanoparticles as a vector for therapy delivery are shown to greatly benefit treatment

outcomes.[102] The semi-automated diffusion barriers model developed in Chapter 2 could be further developed as a graphical user interface and be distributed for use in the clinical setting, especially for use with pathologists and radiologists to help in the identification of positive treatment prediction for breast cancer, in addition to expanding this model to other cancers. The wide use of this model will help to obtain larger data sets to further determine the bounds of the model.

REFERENCES

1. Siegel, R.; Naishadham, D.; Jemal, A. *CA: A Cancer Journal for Clinicians* **2012,** 62, (1), 10-29.
2. Kitano, H. *Nature reviews. Cancer* **2004,** 4, (3), 227-35.
3. Pasquier, J.; Magal, P.; Boulange-Lecomte, C.; Webb, G.; Le Foll, F. *Biology direct* **2011,** 6, 5.
4. Daniel, C.; Bell, C.; Burton, C.; Harguindey, S.; Reshkin, S. J.; Rauch, C. *Biochimica et biophysica acta* **2013,** 1832, (5), 606-17.
5. Garraway, L. A.; Janne, P. A. *Cancer discovery* **2012,** 2, (3), 214-26.
6. Han, H. D.; Lee, A.; Hwang, T.; Song, C. K.; Seong, H.; Hyun, J.; Shin, B. C. *Journal of Controlled Release* **2007,** 120, (3), 161-168.
7. Minchinton, A. I.; Tannock, I. F. *Nature reviews. Cancer* **2006,** 6, (8), 583-592.
8. Tannock, I. F.; Lee, C. M.; Tunggal, J. K.; Cowan, D. S.; Egorin, M. J. *Clinical cancer research : an official journal of the American Association for Cancer Research* **2002,** 8, (3), 878-84.
9. Tredan, O.; Galmarini, C. M.; Patel, K.; Tannock, I. F. *Journal of the National Cancer Institute* **2007,** 99, (19), 1441-54.
10. Cristini, V.; Lowengrub, J., *Multiscale modeling of cancer: an integrated experimental and mathematical modeling approach*. Cambridge University Press: 2010.
11. Hatzikirou, H.; Chauviere, A.; Bauer, A. L.; Leier, A.; Lewis, M. T.; Macklin, P.; Marquez-Lago, T. T.; Bearer, E. L.; Cristini, V. *Wiley Interdisciplinary Reviews: Systems Biology and Medicine* **2012,** 4, (1), 1-14.
12. Marx, V. *Nature* **2013,** 498, (7453), 255-260.
13. Deisboeck, T. S.; Wang, Z.; Macklin, P.; Cristini, V. *Annual review of biomedical engineering* **2011,** 13, 127-55.
14. Lowengrub, J. S.; Frieboes, H. B.; Jin, F.; Chuang, Y. L.; Li, X.; Macklin, P.; Wise, S. M.; Cristini, V. *Nonlinearity* **2010,** 23, (1), R1-R9.
15. Rejniak, K. A.; Anderson, A. R. A. *Wiley interdisciplinary reviews. Systems biology and medicine* **2011,** 3, (1), 115-125.
16. Tracqui, P. *Reports on Progress in Physics* **2009,** 72, (5), 056701.
17. Kim, M.; Gillies, R. J.; Rejniak, K. A. *Frontiers in Oncology* **2013,** 3, 278.
18. Atari, M. I.; Chappell, M. J.; Errington, R. J.; Smith, P. J.; Evans, N. D. *Computer methods and programs in biomedicine* **2011,** 104, (2), 93-103.
19. Lavi, O.; Gottesman, M. M.; Levy, D. *Drug Resistance Updates* **2012,** 15, (1), 90-97.
20. Faratian, D.; Goltsov, A.; Lebedeva, G.; Sorokin, A.; Moodie, S.; Mullen, P.; Kay, C.; Um, I. H.; Langdon, S.; Goryanin, I.; Harrison, D. J. *Cancer research* **2009,** 69, (16), 6713-20.
21. Kirouac, D. C.; Du, J. Y.; Lahdenranta, J.; Overland, R.; Yarar, D.; Paragas, V.; Pace, E.; McDonagh, C. F.; Nielsen, U. B.; Onsum, M. D. *Science signaling* **2013,** 6, (288), ra68.
22. Niepel, M.; Hafner, M.; Pace, E. A.; Chung, M.; Chai, D. H.; Zhou, L.; Schoeberl, B.; Sorger, P. K. *Science signaling* **2013,** 6, (294), ra84.
23. Engel, R. H.; Kaklamani, V. G. *Drugs* **2007,** 67, (9), 1329-41.
24. Romond, E. H.; Perez, E. A.; Bryant, J.; Suman, V. J.; Geyer, C. E., Jr.; Davidson, N. E.; Tan-Chiu, E.; Martino, S.; Paik, S.; Kaufman, P. A.; Swain, S. M.; Pisansky, T. M.; Fehrenbacher, L.; Kutteh, L. A.; Vogel, V. G.; Visscher, D. W.; Yothers, G.; Jenkins, R. B.; Brown, A. M.; Dakhil, S. R.; Mamounas, E. P.; Lingle, W. L.; Klein, P. M.; Ingle, J. N.; Wolmark, N. *The New England journal of medicine* **2005,** 353, (16), 1673-84.
25. Vera, J.; Schmitz, U.; Lai, X.; Engelmann, D.; Khan, F. M.; Wolkenhauer, O.; Putzer, B. M. *Cancer research* **2013,** 73, (12), 3511-24.
26. Roe-Dale, R.; Isaacson, D.; Kupferschmid, M. *Bulletin of mathematical biology* **2011,** 73, (3), 585-608.

27. Tannock, I. F. *Cancer metastasis reviews* **2001,** 20, (1-2), 123-32.
28. Whiteside, T. L. *Oncogene* **2008,** 27, (45), 5904-5912.
29. Koumoutsakos, P.; Pivkin, I.; Milde, F. *Annual review of fluid mechanics* **2013,** 45.
30. Sanga, S.; Sinek, J. P.; Frieboes, H. B.; Ferrari, M.; Fruehauf, J. P.; Cristini, V. *Expert review of anticancer therapy* **2006,** 6, (10), 1361-1376.
31. Stylianopoulos, T.; Martin, J. D.; Chauhan, V. P.; Jain, S. R.; Diop-Frimpong, B.; Bardeesy, N.; Smith, B. L.; Ferrone, C. R.; Hornicek, F. J.; Boucher, Y.; Munn, L. L.; Jain, R. K. *Proceedings of the National Academy of Sciences of the United States of America* **2012,** 109, (38), 15101-15108.
32. Padera, T. P.; Stoll, B. R.; Tooredman, J. B.; Capen, D.; di Tomaso, E.; Jain, R. K. *Nature* **2004,** 427, (6976), 695.
33. Torchilin, V. P. *European Journal of Pharmaceutical Sciences* **2000,** 11, (Supplement 2), S81-S91.
34. Heldin, C. H.; Rubin, K.; Pietras, K.; Ostman, A. *Nature reviews. Cancer* **2004,** 4, (10), 806-13.
35. Jain, R. K.; Stylianopoulos, T. *Nature reviews. Clinical oncology* **2010,** 7, (11), 653-664.
36. Stylianopoulos, T.; Martin, J. D.; Snuderl, M.; Mpekris, F.; Jain, S. R.; Jain, R. K. *Cancer research* **2013,** 73, (13), 3833-3841.
37. Tunggal, J. K.; Cowan, D. S.; Shaikh, H.; Tannock, I. F. *Clinical cancer research : an official journal of the American Association for Cancer Research* **1999,** 5, (6), 1583-6.
38. Grantab, R.; Sivananthan, S.; Tannock, I. F. *Cancer research* **2006,** 66, (2), 1033-9.
39. Jain, R. K. *Cancer research* **1987,** 47, (12), 3039-51.
40. Eisbruch, A.; Shewach, D. S.; Bradford, C. R.; Littles, J. F.; Teknos, T. N.; Chepeha, D. B.; Marentette, L. J.; Terrell, J. E.; Hogikyan, N. D.; Dawson, L. A.; Urba, S.; Wolf, G. T.; Lawrence, T. S. *Journal of clinical oncology : official journal of the American Society of Clinical Oncology* **2001,** 19, (3), 792-9.
41. Taghian, A. G.; Abi-Raad, R.; Assaad, S. I.; Casty, A.; Ancukiewicz, M.; Yeh, E.; Molokhia, P.; Attia, K.; Sullivan, T.; Kuter, I.; Boucher, Y.; Powell, S. N. *Journal of clinical oncology : official journal of the American Society of Clinical Oncology* **2005,** 23, (9), 1951-61.
42. Lankelma, J.; Dekker, H.; Luque, F. R.; Luykx, S.; Hoekman, K.; van der Valk, P.; van Diest, P. J.; Pinedo, H. M. *Clinical cancer research : an official journal of the American Association for Cancer Research* **1999,** 5, (7), 1703-7.
43. Primeau, A. J.; Rendon, A.; Hedley, D.; Lilge, L.; Tannock, I. F. *Clinical cancer research : an official journal of the American Association for Cancer Research* **2005,** 11, (24 Pt 1), 8782-8.
44. Koay, E. J.; Truty, M. J.; Cristini, V.; Thomas, R. M.; Chen, R.; Chatterjee, D.; Kang, Y. a.; Bhosale, P. R.; Tamm, E. P.; Crane, C. H.; Javle, M.; Katz, M. H.; Gottumukkala, V. N.; Rozner, M. A.; Shen, H.; Lee, J. E.; Wang, H.; Chen, Y.; Plunkett, W.; Abbruzzese, J. L.; Wolff, R. A.; Varadhachary, G. R.; Ferrari, M.; Fleming, J. B. *The Journal of Clinical Investigation* **2014,** 124, (4), 1525-1536.
45. Farrell, J. J.; Elsaleh, H.; Garcia, M.; Lai, R.; Ammar, A.; Regine, W. F.; Abrams, R.; Benson, A. B.; Macdonald, J.; Cass, C. E.; Dicker, A. P.; Mackey, J. R. *Gastroenterology* **2009,** 136, (1), 187-195.
46. Sinek, J. P.; Sanga, S.; Zheng, X.; Frieboes, H. B.; Ferrari, M.; Cristini, V. *Journal of Mathematical Biology* **2009,** 58, (4-5), 485-510.
47. Zheng, X.; Wise, S. M.; Cristini, V. *Bulletin of mathematical biology* **2005,** 67, (2), 211-59.
48. Cristini, V.; Bławzdziewicz, J.; Loewenberg, M. *Journal of Computational Physics* **2001,** 168, (2), 445-463.
49. Baish, J. W.; Stylianopoulos, T.; Lanning, R. M.; Kamoun, W. S.; Fukumura, D.; Munn, L. L.; Jain, R. K. *Proceedings of the National Academy of Sciences of the United States of America* **2011,** 108, (5), 1799-1803.
50. Jain, R. K. *Science* **2005,** 307, (5706), 58-62.
51. Thurber, G. M.; Yang, K. S.; Reiner, T.; Kohler, R. H.; Sorger, P.; Mitchison, T.; Weissleder, R. *Nature communications* **2013,** 4, 1504.

52. Stapleton, S.; Milosevic, M.; Allen, C.; Zheng, J.; Dunne, M.; Yeung, I.; Jaffray, D. A. *PLoS ONE* **2013,** 8, (12), e81157.
53. Maeda, H.; Wu, J.; Sawa, T.; Matsumura, Y.; Hori, K. *Journal of Controlled Release* **2000,** 65, (1), 271-284.
54. Wu, M.; Frieboes, H. B.; McDougall, S. R.; Chaplain, M. A. J.; Cristini, V.; Lowengrub, J. *Journal of theoretical biology* **2013,** 320, 131-151.
55. Macklin, P.; McDougall, S.; Anderson, A. R. A.; Chaplain, M. A. J.; Cristini, V.; Lowengrub, J. *Journal of mathematical biology* **2009,** 58, (4-5), 765-798.
56. Stylianopoulos, T.; Soteriou, K.; Fukumura, D.; Jain, R. K. *Annals of biomedical engineering* **2013,** 41, (1), 68-77.
57. Stylianopoulos, T.; Diop-Frimpong, B.; Munn, L. L.; Jain, R. K. *Biophysical Journal* **2010,** 99, (10), 3119-3128.
58. Stylianopoulos, T.; Poh, M.-Z.; Insin, N.; Bawendi, M. G.; Fukumura, D.; Munn, Lance L.; Jain, R. K. *Biophysical Journal* **2010,** 99, (5), 1342-1349.
59. Wise, S. M.; Lowengrub, J. S.; Frieboes, H. B.; Cristini, V. *Journal of theoretical biology* **2008,** 253, (3), 524-543.
60. Frieboes, H. B.; Edgerton, M. E.; Fruehauf, J. P.; Rose, F. R. A. J.; Worrall, L. K.; Gatenby, R. A.; Ferrari, M.; Cristini, V. *Cancer research* **2009,** 69, (10), 4484-4492.
61. Das, H.; Wang, Z.; Niazi, M. K. K.; Aggarwal, R.; Lu, J.; Kanji, S.; Das, M.; Joseph, M.; Gurcan, M.; Cristini, V. *PLoS ONE* **2013,** 8, (4), e61398.
62. Pascal, J.; Bearer, E. L.; Wang, Z.; Koay, E. J.; Curley, S. A.; Cristini, V. *Proceedings of the National Academy of Sciences of the United States of America* **2013,** 110, (35), 14266-14271.
63. Gillies, R. J.; Schornack, P. A.; Secomb, T. W.; Raghunand, N. *Neoplasia (New York, N.Y.)* **1999,** 1, (3), 197-207.
64. Vaupel, P. In *Tumor microenvironmental physiology and its implications for radiation oncology*, Seminars in radiation oncology, 2004; Elsevier: pp 198-206.
65. Gerweck, L. E.; Vijayappa, S.; Kozin, S. *Mol Cancer Ther* **2006,** 5, (5), 1275-9.
66. Tannock, I. F.; Rotin, D. *Cancer research* **1989,** 49, (16), 4373-84.
67. Shah, M. A.; Schwartz, G. K. *Clinical cancer research : an official journal of the American Association for Cancer Research* **2001,** 7, (8), 2168-81.
68. Venkatasubramanian, R.; Henson, M. A.; Forbes, N. S. *J Theor Biol* **2006,** 242, (2), 440-53.
69. Venkatasubramanian, R.; Henson, M. A.; Forbes, N. S. *Journal of theoretical biology* **2008,** 253, (1), 98-117.
70. Blanco, E.; Ferrari, M. *The Breast* **2014,** 23, (1), 10-18.
71. Frieboes, H. B.; Wu, M.; Lowengrub, J.; Decuzzi, P.; Cristini, V. *PLoS ONE* **2013,** 8, (2), e56876.
72. Pascal, J.; Ashley, C. E.; Wang, Z.; Brocato, T. A.; Butner, J. D.; Carnes, E. C.; Koay, E. J.; Brinker, C. J.; Cristini, V. *ACS nano* **2013,** 7, (12), 11174-11182.
73. Van De Ven, A. L.; Wu, M.; Lowengrub, J.; McDougall, S. R.; Chaplain, M. A.; Cristini, V.; Ferrari, M.; Frieboes, H. B. *AIP advances* **2012,** 2, (1), 011208.
74. Susa, M.; Iyer, A. K.; Ryu, K.; Hornicek, F. J.; Mankin, H.; Amiji, M. M.; Duan, Z. *BMC Cancer* **2009,** 9, 399-399.
75. Miller, K. D.; Siegel, R. L.; Lin, C. C.; Mariotto, A. B.; Kramer, J. L.; Rowland, J. H.; Stein, K. D.; Alteri, R.; Jemal, A. *CA: A Cancer Journal for Clinicians* **2016,** 66, (4), 271-289.
76. Wolmark, N.; Wang, J.; Mamounas, E.; Bryant, J.; Fisher, B. *JNCI Monographs* **2001,** 2001, (30), 96-102.
77. Fisher, B.; Bryant, J.; Wolmark, N.; Mamounas, E.; Brown, A.; Fisher, E. R.; Wickerham, D. L.; Begovic, M.; DeCillis, A.; Robidoux, A.; Margolese, R. G.; Jr, A. B. C.; Hoehn, J. L.; Lees, A. W.; Dimitrov, N. V.; Bear, H. D. *Journal of Clinical Oncology* **1998,** 16, (8), 2672-2685.

78. Mittendorf, E. A.; Jeruss, J. S.; Tucker, S. L.; Kolli, A.; Newman, L. A.; Gonzalez-Angulo, A. M.; Buchholz, T. A.; Sahin, A. A.; Cormier, J. N.; Buzdar, A. U.; Hortobagyi, G. N.; Hunt, K. K. *Journal of Clinical Oncology* **2011,** 29, (15), 1956-1962.
79. van der Hage, J. H.; van de Velde, C. C. J. H.; Mieog, S. J. S. D. *Cochrane Database of Systematic Reviews* **2007**, (2).
80. Ellis, G. K.; Barlow, W. E.; Gralow, J. R.; Hortobagyi, G. N.; Russell, C. A.; Royce, M. E.; Perez, E. A.; Lew, D.; Livingston, R. B. *Journal of Clinical Oncology* **2011,** 29, (8), 1014-1021.
81. Mahmoud, S. M. A.; Paish, E. C.; Powe, D. G.; Macmillan, R. D.; Grainge, M. J.; Lee, A. H. S.; Ellis, I. O.; Green, A. R. *Journal of Clinical Oncology* **2011,** 29, (15), 1949-1955.
82. Denkert, C.; Minckwitz, G.; Brase, J. C.; Sinn, B. V.; Gade, S.; Kronenwett, R. *Journal of clinical oncology : official journal of the American Society of Clinical Oncology* **2015,** 33.
83. Denkert, C.; Loibl, S.; Noske, A.; Roller, M.; Muller, B. M.; Komor, M. *Journal of clinical oncology : official journal of the American Society of Clinical Oncology* **2010,** 28.
84. Denkert, C.; Loibl, S.; Noske, A.; Roller, M.; Müller, B. M.; Komor, M.; Budczies, J.; Darb-Esfahani, S.; Kronenwett, R.; Hanusch, C.; Törne, C. v.; Weichert, W.; Engels, K.; Solbach, C.; Schrader, I.; Dietel, M.; Minckwitz, G. v. *Journal of Clinical Oncology* **2010,** 28, (1), 105-113.
85. Ali, H. R.; Dariush, A.; Provenzano, E.; Bardwell, H.; Abraham, J. E.; Iddawela, M.; Vallier, A.-L.; Hiller, L.; Dunn, J. A.; Bowden, S. J.; Hickish, T.; McAdam, K.; Houston, S.; Irwin, M. J.; Pharoah, P. D. P.; Brenton, J. D.; Walton, N. A.; Earl, H. M.; Caldas, C. *Breast Cancer Research* **2016,** 18, (1), 21.
86. Pascal, J.; Bearer, E. L.; Wang, Z.; Koay, E. J.; Curley, S. A.; Cristini, V. *Proceedings of the National Academy of Sciences* **2013,** 110, (35), 14266-14271.
87. Das, H.; Wang, Z.; Niazi, M. K.; Aggarwal, R.; Lu, J.; Kanji, S.; Das, M.; Joseph, M.; Gurcan, M.; Cristini, V. *PloS one* **2013,** 8, (4), e61398.
88. Koay, E. J.; Truty, M. J.; Cristini, V.; Thomas, R. M.; Chen, R.; Chatterjee, D.; Kang, Y.; Bhosale, P. R.; Tamm, E. P.; Crane, C. H.; Javle, M.; Katz, M. H.; Gottumukkala, V. N.; Rozner, M. A.; Shen, H.; Lee, J. E.; Wang, H.; Chen, Y.; Plunkett, W.; Abbruzzese, J. L.; Wolff, R. A.; Varadhachary, G. R.; Ferrari, M.; Fleming, J. B. *J Clin Invest* **2014,** 124, (4), 1525-36.
89. Frieboes, H. B.; Smith, B. R.; Wang, Z.; Kotsuma, M.; Ito, K.; Day, A.; Cahill, B.; Flinders, C.; Mumenthaler, S. M.; Mallick, P.; Simbawa, E.; Al-Fhaid, A. S.; Mahmoud, S. R.; Gambhir, S. S.; Cristini, V. *PloS one* **2015,** 10, (6), e0129433.
90. Wang, Z.; Kerketta, R.; Chuang, Y. L.; Dogra, P.; Butner, J. D.; Brocato, T. A.; Day, A.; Xu, R.; Shen, H.; Simbawa, E.; Al-Fhaid, A. S.; Mahmoud, S. R.; Curley, S. A.; Ferrari, M.; Koay, E. J.; Cristini, V. *PLoS computational biology* **2016,** 12, (6), e1004969.
91. Cristini, V.; Koay, E.; Wang, Z., *An Introduction to Physical Oncology: How Mechanistic Mathematical Modeling Can Improve Cancer Therapy Outcomes*. CRC Press: 2017.
92. Edgerton, M. E.; Chuang, Y.-L.; Macklin, P.; Yang, W.; Bearer, E. L.; Cristini, V. *Analytical Cellular Pathology* **2011,** 34, (5), 247-263.
93. Adiseshaiah, P. P.; Crist, R. M.; Hook, S. S.; McNeil, S. E. *Nature reviews. Clinical oncology* **2016,** 13, (12), 750-765.
94. Pickles, M. D.; Manton, D. J.; Lowry, M.; Turnbull, L. W. *European Journal of Radiology* **2009,** 71, (3), 498-505.
95. Pickles, M. D.; Lowry, M.; Manton, D. J.; Gibbs, P.; Turnbull, L. W. *Breast Cancer Research and Treatment* **2005,** 91, (1), 1-10.
96. Nagy, J. A.; Chang, S. H.; Dvorak, A. M.; Dvorak, H. F. *British Journal of Cancer* **2009,** 100, (6), 865-869.
97. Zöllner, F. G.; Daab, M.; Sourbron, S. P.; Schad, L. R.; Schoenberg, S. O.; Weisser, G. *BMC Medical Imaging* **2016,** 16, (1), 7.
98. Siegel, R. L.; Miller, K. D.; Jemal, A. *CA: A Cancer Journal for Clinicians* **2015,** 65, (1), 5-29.

99. Chakrabarti, A.; Verbridge, S.; Stroock, A.; Fischbach, C.; Varner, J. *Ann Biomed Eng* **2012,** 40, (11), 2488-2500.
100. Tang, D. G. *Cell Res* **2012,** 22, (3), 457-472.
101. Hanessian, S.; Grzyb, J. A.; Cengelli, F.; Juillerat-Jeanneret, L. *Bioorganic & Medicinal Chemistry* **2008,** 16, (6), 2921-2931.
102. Durfee, P. N.; Lin, Y.-S.; Dunphy, D. R.; Muñiz, A. J.; Butler, K. S.; Humphrey, K. R.; Lokke, A. J.; Agola, J. O.; Chou, S. S.; Chen, I. M.; Wharton, W.; Townson, J. L.; Willman, C. L.; Brinker, C. J. *ACS Nano* **2016,** 10, (9), 8325-8345.
103. Townson, J. L.; Lin, Y.-S.; Agola, J. O.; Carnes, E. C.; Leong, H. S.; Lewis, J. D.; Haynes, C. L.; Brinker, C. J. *Journal of the American Chemical Society* **2013,** 135, (43), 16030-16033.
104. Butler, K. S.; Durfee, P. N.; Theron, C.; Ashley, C. E.; Carnes, E. C.; Brinker, C. J. *Small* **2016,** 12, (16), 2173-2185.
105. Wu, X.; Wu, M.; Zhao, J. X. *Nanomedicine: Nanotechnology, Biology and Medicine* **2014,** 10, (2), 297-312.
106. Krol, S.; Macrez, R.; Docagne, F.; Defer, G.; Laurent, S.; Rahman, M.; Hajipour, M. J.; Kehoe, P. G.; Mahmoudi, M. *Chemical reviews* **2013,** 113, (3), 1877-903.
107. Li, Z.; Barnes, J. C.; Bosoy, A.; Stoddart, J. F.; Zink, J. I. *Chemical Society Reviews* **2012,** 41, (7), 2590-2605.
108. Modo, M.; Mellodew, K.; Cash, D.; Fraser, S. E.; Meade, T. J.; Price, J.; Williams, S. C. *NeuroImage* **2004,** 21, (1), 311-7.
109. Vuu, K.; Xie, J.; McDonald, M. A.; Bernardo, M.; Hunter, F.; Zhang, Y.; Li, K.; Bednarski, M.; Guccione, S. *Bioconjugate Chemistry* **2005,** 16, (4), 995-999.
110. Chen, F.; Nayak, T. R.; Goel, S.; Valdovinos, H. F.; Hong, H.; Theuer, C. P.; Barnhart, T. E.; Cai, W. *Molecular Pharmaceutics* **2014,** 11, (11), 4007-4014.
111. Shi, S.; Chen, F.; Cai, W. *Nanomedicine* **2013,** 8, 2027+.
112. Huang, H.; Cui, X. X.; Chen, S.; Goodin, S.; Liu, Y.; He, Y.; Li, D.; Wang, H.; Van Doren, J.; Dipaola, R. S.; Conney, A. H.; Zheng, X. *Anticancer research* **2014,** 34, (7), 3357-63.
113. Abdelwahab, M. G.; Sankar, T.; Preul, M. C.; Scheck, A. C. *Journal of Visualized Experiments : JoVE* **2011**, (57), 3403.
114. Medina-Ramirez, C. M.; Goswami, S.; Smirnova, T.; Bamira, D.; Benson, B.; Ferrick, N.; Segall, J.; Pollard, J. W.; Kitsis, R. N. *Cancer research* **2011,** 71, (24), 7705-15.
115. Cherry, S. R. *Seminars in nuclear medicine* **2009,** 39, (5), 348-353.
116. Chen, F.; Hong, H.; Zhang, Y.; Valdovinos, H. F.; Shi, S.; Kwon, G. S.; Theuer, C. P.; Barnhart, T. E.; Cai, W. *ACS Nano* **2013,** 7, (10), 9027-9039.
117. Alric, C.; Taleb, J.; Duc, G. L.; Mandon, C.; Billotey, C.; Meur-Herland, A. L.; Brochard, T.; Vocanson, F.; Janier, M.; Perriat, P.; Roux, S.; Tillement, O. *Journal of the American Chemical Society* **2008,** 130, (18), 5908-5915.
118. Wang, Z. H.; Kerketta, R.; Chuang, Y. L.; Dogra, P.; Butner, J. D.; Brocato, T. A.; Day, A.; Xu, R.; Shen, H. F.; Simbawa, E.; Al-Fhaid, A. S.; Mahmoud, S. R.; Curley, S. A.; Ferrari, M.; Koay, E. J.; Cristini, V. *Plos Computational Biology* **2016,** 12, (6).
119. Arami, H.; Khandhar, A.; Liggitt, D.; Krishnan, K. M. *Chemical Society Reviews* **2015,** 44, (23), 8576-8607.
120. Miller, J. W.; Royalty, J.; Henley, J.; White, A.; Richardson, L. C. *Cancer causes & control : CCC* **2015,** 26, (5), 741-7.
121. Monteiro-Riviere, N. A.; Tran, C. L., *Nanotoxicology: progress toward nanomedicine*. CRC press: 2014; p 178.
122. Noremberg, S.; Veiga, M.; Bohrer, D.; Viana, C.; Cicero do Nascimento, P.; Machado de Carvalho, L.; Mattiazzi, P. *Analytical Methods* **2015,** 7, (2), 500-506.

123. Wilhelm, S.; Tavares, A. J.; Dai, Q.; Ohta, S.; Audet, J.; Chan, W. C. W.; Dvorak, H. F. *Nature Reviews Materials* **2016,** 1.
124. Meng, H.; Xue, M.; Xia, T.; Ji, Z.; Tarn, D. Y.; Zink, J. I.; Nel, A. E. *ACS Nano* **2011,** 5, (5), 4131-4144.
125. Chakravarty, R.; Goel, S.; Hong, H.; Chen, F.; Valdovinos, H. F.; Hernandez, R.; Barnhart, T. E.; Cai, W. *Nanomedicine (London, England)* **2015,** 10, (8), 1233-46.
126. Benezra, M.; Penate-Medina, O.; Zanzonico, P. B.; Schaer, D.; Ow, H.; Burns, A.; DeStanchina, E.; Longo, V.; Herz, E.; Iyer, S.; Wolchok, J.; Larson, S. M.; Wiesner, U.; Bradbury, M. S. *J Clin Invest* **2011,** 121, (7), 2768-80.
127. Bimbo, L. M.; Denisova, O. V.; Makila, E.; Kaasalainen, M.; De Brabander, J. K.; Hirvonen, J.; Salonen, J.; Kakkola, L.; Kainov, D.; Santos, H. A. *ACS Nano* **2013,** 7, (8), 6884-93.
128. Kovalainen, M.; Monkare, J.; Kaasalainen, M.; Riikonen, J.; Lehto, V. P.; Salonen, J.; Herzig, K. H.; Jarvinen, K. *Mol Pharm* **2013,** 10, (1), 353-9.
129. McInnes, S. J.; Irani, Y.; Williams, K. A.; Voelcker, N. H. *Nanomedicine (Lond)* **2012,** 7, (7), 995-1016.
130. Bharti, C.; Nagaich, U.; Pal, A. K.; Gulati, N. *International journal of pharmaceutical investigation* **2015,** 5, (3), 124-33.
131. Curtis, L. T.; Wu, M.; Lowengrub, J.; Decuzzi, P.; Frieboes, H. B. *PLOS ONE* **2015,** 10, (12), e0144888.
132. Ashley, C. E.; Carnes, E. C.; Phillips, G. K.; Padilla, D.; Durfee, P. N.; Brown, P. A.; Hanna, T. N.; Liu, J.; Phillips, B.; Carter, M. B.; Carroll, N. J.; Jiang, X.; Dunphy, D. R.; Willman, C. L.; Petsev, D. N.; Evans, D. G.; Parikh, A. N.; Chackerian, B.; Wharton, W.; Peabody, D. S.; Brinker, C. J. *Nature materials* **2011,** 10, (5), 389-97.
133. Stein, W. D.; Gulley, J. L.; Schlom, J.; Madan, R. A.; Dahut, W.; Figg, W. D.; Ning, Y.-m.; Arlen, P. M.; Price, D.; Bates, S. E.; Fojo, T. *Clinical Cancer Research* **2011,** 17, (4), 907-917.
134. Miccò, M.; Vargas, H. A.; Burger, I. A.; Kollmeier, M. A.; Goldman, D. A.; Park, K. J.; Abu-Rustum, N. R.; Hricak, H.; Sala, E. *European Journal of Radiology* **2014,** 83, (7), 1169-1176.
135. Lin, Y.-S.; Abadeer, N.; Hurley, K. R.; Haynes, C. L. *Journal of the American Chemical Society* **2011,** 133, (50), 20444-20457.
136. Tsai, P. P.; Pachowsky, U.; Stelzer, H. D.; Hackbarth, H. *Laboratory animals* **2002,** 36, (4), 411-9.